American Mineralogist, Volume 100, pages 1355–1377, 2015

PRESIDENTIAL ADDRESS

SPECIAL COLLECTION: NANOMINERALS AND MINERAL NANOPARTICLES

Nano- and micro-geochronology in Hadean and Archean zircons by atom-probe tomography and SIMS: New tools for old minerals†

JOHN W. VALLEY[1,2,*], DAVID A. REINHARD[3], AARON J. CAVOSIE[1,2,4,‡], TAKAYUKI USHIKUBO[1,§], DANIEL F. LAWRENCE[3], DAVID J. LARSON[3], THOMAS F. KELLY[3], DAVID R. SNOEYENBOS[5] AND ARIEL STRICKLAND[1]

[1]WiscSIMS, Department of Geoscience, University of Wisconsin, Madison, Wisconsin 53706, U.S.A.
[2]NASA Astrobiology Institute, Department of Geoscience, University of Wisconsin, Madison, Wisconsin 53706, U.S.A.
[3]CAMECA Instruments, Madison, Wisconsin 53711, U.S.A.
[4]Department of Geology, University of Puerto Rico, Mayaguez, Puerto Rico 00681, U.S.A.
[5]Department of Geosciences, University of Massachusetts, Amherst, Massachusetts 01003, U.S.A.

ABSTRACT

Atom-probe tomography (APT) and secondary ion mass spectrometry (SIMS) provide complementary in situ element and isotope data in minerals such as zircon. SIMS measures isotope ratios and trace elements from 1–20 μm spots with excellent accuracy and precision. APT identifies mass/charge and three-dimensional position of individual atoms (±0.3 nm) in 100 nm-scale samples, volumes up to one million times smaller than SIMS. APT data provide unique information for understanding element and isotope distribution; crystallization and thermal history; and mechanisms of mineral reaction and exchange. This atomistic view enables evaluation of the fidelity of geochemical data for zircon because it provides new understanding of radiation damage, and can test for intracrystalline element mobility. Nano-geochronology is one application of APT in which Pb isotope ratios from sub-micrometer domains of zircon provide model ages of crystallization and identify later magmatic and metamorphic reheating.

Based on SEM imaging and SIMS analysis, 11 needle-shaped specimens ~100 nm in diameter were sampled from one Archean and two Hadean zircons by focused ion-beam milling and analyzed with APT. The three-dimensional distribution of Pb and nominally incompatible elements (Y, REEs) differs at the atomic scale in each zircon. Zircon JH4.0 (4.007 Ga, Jack Hills, Western Australia) is homogeneous in Pb, Y, and REEs. In contrast, Pb and Y and REEs are clustered in sub-equant ~10 nm diameter domains, spaced 10–40 nm apart in zircons ARG2.5 (2.542 Ga, Grouse Creek Mountains, Utah) and JH4.4 (4.374 Ga, Jack Hills). Most clusters are flattened parallel to (100) or (010). U and Th are not collocated with Pb in clusters and appear to be homogeneously distributed in all three zircons. The analyzed domains experienced 4 to 8×10^{15} α-decay events/mg due to U and Th decay and yet all zircons yield U-Pb ages by SIMS that are better than 97% concordant, consistent with annealing of most radiation damage. The $^{207}Pb/^{206}Pb$ ratios for the 100 nm-scale specimens measured by APT average 0.17 for ARG2.5, 0.42 for the JH4.0, and 0.52 for JH4.4. These ratios are less precise (±10–18% 2σ) due to the ultra-small sample size, but in excellent agreement with values measured by SIMS (0.1684, 0.4269, and 0.5472, respectively) and the crystallization ages of the zircons. Thus Pb in these clusters is radiogenic, but unsupported, meaning that the Pb is not spatially associated with its parent isotopes of U and Th. For the domain outside of clusters in JH4.4, the $^{207}Pb/^{206}Pb$ ratio is 0.3, consistent with the SIMS value of 0.2867 for the zircon overgrowth rim and an age of 3.4 Ga. In ARG2.5, all Pb is concentrated in clusters and there is no detectable Pb remaining outside of the clusters. The Pb-Y-REE-rich clusters and lack of correlation with U in ARG2.5 and JH4.4 are best explained by diffusion of Pb and other elements into ~10 nm amorphous domains formed by α-recoil. Diffusion distances of ~20 nm for these elements in crystalline zircon are consistent with heating at temperatures of 800 °C for ~2 m.y. Such later reheating events are identified and dated by APT from $^{207}Pb/^{206}Pb$ model ages of clusters in JH4.4 and by the absence of detectable Pb outside of clusters in ARG2.5. SIMS dates

* E-mail: valley@geology.wisc.edu
‡ Present address: Department of Applied Geology, Curtin University, Perth 6102, Australia.
§ Present address: Kochi Institute for Core Sample Research, JAMSTEC, Nankoku, Kochi 783-8502, Japan.
† Open access: Article available to all readers online. Special collection papers can be found on GSW at http://ammin.geoscienceworld.org/site/misc/specialissuelist.xhtml.

0003-004X/15/0007–1355$05.00/DOI: http://dx.doi.org/10.2138/am-2015-5134

for the zircon rims independently confirm reheating of ARG2.5 and JH4.4, which were xenocrysts in younger magmas when rims formed. It is proposed that most domains damaged by α-recoil were annealed at ambient temperatures above 200–300 °C before reheating and only a small number of domains were amorphous and available to concentrate Pb at the time of reheating. The size, shapes, and orientations of clusters were altered by annealing after formation. The absence of enriched clusters in JH4.0 shows that this zircon was not similarly reheated. Thus APT data provide thermochronologic information about crustal reworking even for zircons where no overgrowth is recognized. The clusters in JH4.4 document Pb mobility at the sub-50 nm scale, but show that the much larger 20 μm-scale domains analyzed by SIMS were closed systems. The reliability of oxygen isotope ratios and other geochemical data from zircon can be evaluated by these means. These results verify the age of this zircon and support previous proposals that differentiated crust existed by 4.4 Ga and that the surface of Earth was relatively cool with habitable oceans before 4.3 Ga. These analytical techniques are of general applicability to minerals of all ages and open many new research opportunities.

Keywords: Atom-probe tomography, APT, radiation damage, SIMS, zircon, nano-geochronology, oxygen isotopes, Hadean

Introduction

Atom-probe tomography (APT) is an analytical tool that has only recently become available for studies of electrically insulating phases including silicate minerals. In terms of spatial resolution and detection limits for chemical analysis, the capabilities are intermediate between secondary ion mass spectrometry (SIMS) and transmission electron microscopy (TEM) (Fig. 1; Gault et al. 2012). Similar to TEM, sample sizes are at the 100 nm-scale and individual atoms are routinely located in three dimensions. Like SIMS, atoms can be identified and isotope ratios measured. No other technique provides spatially resolved mass spectrometry and three-dimension mapping at single-atom scale. The complementary application of APT and SIMS to zircons offers unique opportunities to assess sample heterogeneity, radiation damage, and element mobility, issues that U-Pb geochronologists have wrestled with for 100 years.

Less than 20 years after the discovery of radioactivity, Holmes (1913) estimated the age of the Earth based on decay of U to Pb. Although limited by the technology and understanding of his day, this pioneering work laid the foundations for modern geochronology and identified many critical aspects including the retentiveness of zircon, the closed-system criteria, and possible Pb mobility. Geochronology has progressed greatly since Holmes' first studies (Condon and Schmitz 2013), but the effects of radiation damage, annealing, and Pb mobility in zircon remain poorly understood at the atomic scale.

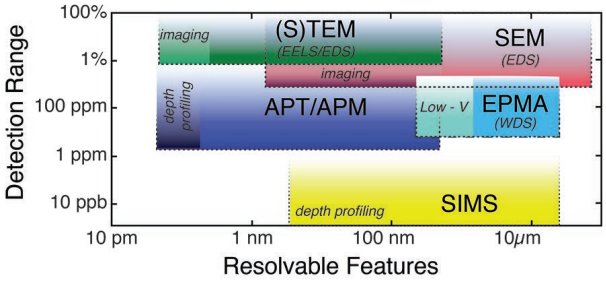

Figure 1. Commonly achieved spatial resolution and detection range for microanalysis. APM = atom probe microscopy; APT = atom probe tomography; EDS = energy-dispersive X-ray spectrometry; EELS = electron energy loss spectroscopy; EPMA = electron-probe microanalysis; SEM = scanning electron microscopy; SIMS = secondary ion mass spectrometry; (S)TEM = (scanning) transmission electron microscopy; WDS = wavelength-dispersive X-ray spectrometry. Modified from Gault et al. (2012).

The effects of radiation damage on bulk properties of zircon were first systematically studied by Holland and Gottfried (1955) and include increases in volume, water content, and dissolution rate; and decreases in birefringence, elastic moduli, and hardness (see Ewing et al. 2003). In extreme cases, metamict zircon is fully altered to a glass-like material. The degree of radiation damage also strongly influences diffusion and exchange rates, and thus the fidelity of geochemical data from zircons. Radioactivity, the very property that makes zircons prized for geochronology, is also its Achilles' heel.

All natural zircons are damaged by radiation at some level. There are many causes including fission tracks, β and α emission, and α-recoil. The recoil of a newly formed daughter atom upon emission of an α-particle (α-recoil) is the dominant cause of damage to the zircon crystal structure. The degree of radiation damage in any sub-domain of zircon will fall along a continuum depending on composition, age, and healing. Following Murakami et al. (1991), the gradations of damage can be described by percolation theory (Salje et al. 1999; Ewing et al. 2003). For low doses of radiation, the damaged domains are isolated. In this state, the grain is said to be below the first percolation point and crystalline zircon surrounds the damaged volumes, potentially armoring them from exchange. The first percolation point (~2×10^{15} α-decays/mg; Rios et al. 2000; Pidgeon 2014) represents the condition where damaged domains overlap to form continuous pathways throughout the crystal (or sub-domain) of interest. At this point, amorphous domains constitute 30–40% by volume and rates of exchange are greatly enhanced in comparison to volume diffusion, which is slow in crystalline zircon (Cherniak 2010).

The increasing use of in situ techniques for spot analysis of sub-domains of a zircon reinforces the importance of evaluating the localized effects of radiation damage, which can facilitate elemental and isotopic exchange and cause erroneous results for measurements of U-Pb age (Ewing et al. 2003; Cavosie et al. 2004; White and Ireland 2012); oxygen isotope ratios (Valley et al. 1994; Valley 2003; Cavosie et al. 2005; Booth et al. 2005; Gao et al. 2014; Wang et al. 2014), and trace elements

(Hoskin and Schaltegger 2003; Cavosie et al. 2006). Just as the concentrations of U and Th can be strongly zoned within a crystal, altered radiation-damage domains may be localized within pristine crystalline zircon at a sub-grain scale (Nasdala et al. 1996; Chakoumakos et al. 1987; Palenik et al. 2003).

Geochemists have employed a wide range of procedures to evaluate radiation damage and the fidelity of zircon data. For multi-grain samples, low-magnetism zircons are readily concentrated and typically contain less U, Th, and rare earth elements (REEs), and have less damage. Low-magnetism zircons yield more concordant ages (Silver 1963; Silver and Deutsch 1963; Krogh 1982) and primary $\delta^{18}O$ values (Valley et al. 1994; Valley 2003). Likewise, soaking in HF removes metamict zircon from a mineral concentrate, which results in improved oxygen isotope data (King et al. 1998), but can leach Pb from damaged domains. The chemical abrasion method for U-Pb analysis employs high-temperature annealing followed by a series of partial dissolution steps to remove progressively less damaged material (Mattinson 2005). For in situ studies of polished surfaces in zircon, domains of questionable reliability can be identified by a range of imaging techniques including: optical examination for micro-cracks, porous zircon, anomalous inclusions, or reduced birefringence; cathodoluminescence imaging (CL), backscattered electron imaging (BSE), and electron backscatter diffraction (EBSD) in a scanning electron microscope (SEM); IR or laser Raman spectroscopy; and fuming with HF (Krogh and Davis 1975; Pidgeon 1992; Zhang et al. 2002; Corfu et al. 2003; Nasdala et al. 2003; Reddy et al. 2006). Radiation damage can also be imaged by HR-TEM (Chakoumakos et al. 1987; Miller and Ewing 1993; Weber et al. 1994; Ewing et al. 2003; Palenik et al. 2003; Utsunomiya et al. 2004, 2007). Likewise, SIMS analysis can identify pristine domains that yield concordant ages and low concentrations of non-formula elements such as Ca, Fe, and Al (Krogh and Davis 1975; Geisler and Schleicher 2000; Rayner et al. 2005; Cavosie et al. 2006; Geisler et al. 2007; Bouvier et al. 2012), and multiple analyses for different isotope systems can be correlated to zoning patterns (Cavosie et al. 2006). One promising new approach is to monitor the molecular ion, $^{16}O^{1}H$, during SIMS analysis of $^{18}O/^{16}O$ as a guide to water content, which may correlate to radiation damage (Pidgeon et al. 2013; Wang et al. 2014). It is always good to look at zircons carefully by a range of techniques before analysis, however, the above procedures provide only an indirect measurement of properties that may correlate to alteration. No previous study has chemically or isotopically analyzed alteration of zircon at the atomic scale.

The interpretation of dates and other data for Archean and Hadean zircons requires special attention to radiation damage. Hadean zircons have been found only as detrital grains or xenocrysts and are the oldest known samples from the early Earth. Determination of their origins is critically dependent on establishing primary magmatic composition. Hadean zircons, even with low [U] and [Th], below a few hundreds of part per million, experience enough α-decay to exceed the first percolation point if not annealed. Fortunately for geochemists, radiation damage has been partially healed in many zircons and primary compositions are reliably preserved. However, uncertainty about post-crystallization modification has fueled challenges to the ages and the fidelity of geochemical data, especially for Archean and Hadean zircons (Ashwal et al. 1999; Nelson et al. 2000; Whitehouse and Kamber 2002; Parrish and Noble 2003; Hoskin and Schaltegger 2003; Hoskin 2005; Nemchin et al. 2006; Holden et al. 2009; Kusiak et al. 2013a, 2013b).

In this study, we used various imaging and microanalysis protocols by SEM and SIMS to select one Archean and two Hadean zircons for APT (Valley et al. 2014a). The combination of APT and SIMS provides an unprecedented record of the atom-scale distribution of isotopes and mobility of trace elements, including Pb, within the zircons. These techniques allow direct measurement of the effects of radiation damage and establish criteria for distinguishing primary vs. altered zircon compositions. In addition, the thermochronology of crystallization and cryptic reheating events, measurable by no other method, is assessed for sub-micrometer domains within each zircon.

Methods

The three zircons in this study were analyzed in multiple sessions at five different secondary ion mass spectrometry (SIMS) laboratories to determine U-Pb age, stable isotope ratios, and trace element composition. JH4.4 was dated by SHRIMP-II at the Chinese Academy of Geological Sciences, Beijing (Cavosie et al. 2004) and at Curtin University (Cavosie et al. 2007). JH4.0 was dated at Curtin University (Cavosie 2005). ARG2.5 was dated by SHRIMP-RG at the Stanford/USGS Micro-Analysis Center (Strickland et al. 2011a).

SHRIMP-II methodology has been described previously (Williams 1998; Cavosie et al. 2004). Age determinations involved 7 measurement cycles for each mass, and were calibrated using the zircon U-Pb standard CZ3 (Pidgeon et al. 1994). Grains of CZ3 were located within the same epoxy mount as the sample. Multiple analyses of CZ3 were made, using a "bracketing strategy," whereby standard analyses were before, during, and after sample analyses. Data were reduced using the program Squid (Ludwig 2001a); sample analyses were corrected for common Pb using measured ^{204}Pb. The 2σ uncertainty in the mean of the Pb/U ratio for the standard analyses was 0.55% for JH4.4 and 0.57% for JH4.0. Graphical representations of the U-Pb data were prepared using the program Isoplot (Ludwig 2001b).

SHRIMP-RG methodology was described in Strickland et al. (2011a). Secondary ions were generated with an O_2^- primary ion beam varying from 2–6 nA. The number of scans through the mass sequence was typically 5–7. Concentration data for zircons were standardized against zircon standard VP-10 (1200 Ma, granitoid, Joshua Tree National Park, Barth and Wooden, unpublished) which was analyzed repeatedly throughout the duration of the analytical session. Data reduction follows the methods described by Williams (1998) and Ireland and Williams (2003) and uses the Squid and Isoplot programs.

Oxygen isotope ratios were measured by IMS 1270 at the University of Edinburgh ($\delta^{18}O$, Cavosie et al. 2005) and by IMS 1280 at WiscSIMS, UW-Madison ($\delta^{18}O$, $\delta^{17}O$, Valley et al. 2007, 2014a; Ushikubo et al. 2008). Techniques are described in those papers and by Kita et al. (2009) and Valley and Kita (2009). Trace elements were measured by IMS 4f in Edinburgh (Cavosie et al. 2006) and IMS 1280 at WiscSIMS (this study). A total of 25 trace elements were analyzed in situ by SIMS (Table 1): Li, Al, P, Ca, Ti, V, Fe, Y, La, Ce, Pr, Nd, Sm, Eu, Gd, Tb, Dy, Ho, Er, Tm, Yb, Lu, Hf, Th, and U using procedures described previously (Page et al. 2007; Fu et al. 2008; Ushikubo et al. 2008). Measurements at WiscSIMS also include $\delta^{7}Li$ (Ushikubo et al. 2008; Bouvier et al. 2012).

Atom-probe tomography

Atom-probe tomography (APT) was conducted using a LEAP 4000X HR at the CAMECA Atom Probe Technology Center, Madison, Wisconsin, where the instrument was manufactured. Zircon slices measuring approximately 3 × 5 × 30 μm were removed from polished surfaces of each crystal and milled to make multiple needle-shaped specimens using a focused ion beam (FIB) guided by cathodoluminescence (CL) and field-emission SEM (Figs. 2a–2d) (Larson et al. 2013a). Six specimens are potentially obtained from each FIB lift-out with final dimensions of ~100 nm at the specimen tip and analyzable lengths of up to

TABLE 1. Trace element analyses (ppm wt.) by SIMS and APT of zircons JH4.4, JH4.0, and ARG2.5

Zircon	JH4.4[3]	JH4.4[3]	JH4.4[3]	JH4.4[3]	JH4.4[4]	JH4.4[4]	JH4.0[2]	JH4.0[2]	ARG2.5[1]	ARG2.5[1]	JH4.4[3]
Spot	TE1	TE2	TE3	TE4	TE5	TE6	TE7	TE8	TE9	TE10	APT
	Core	Core	Rim	Core	Surface2	Surface2	Mantle	Mantle	Core	Mantle	Clusters
Li	6.2	24.2	29.3	20.5			56.2	45.2	0.4	1	6
Al	8.5	11.6	5.4	12.1					40.9	25.5	200
P	222	214	112	288	407	237	166	196	252	183	1600
Ca	0.1	0.2	0.4	6.0			3.6	3.1	2.7	4	30
Ti	13.2	18.4	2.5	10.0			6.1	7.7	12.9	16.8	
V	0.1	0.1	0.02	0.1			0.06	0.02	1.4	0.4	
Fe	45.6	62.5	7.4	39.8			107.3	44.3	6.3	1.5	
Y	3133	3528	226	2508	2869	977	418	454	790	342	105000
La	0.08	0.03	0.002	0.05	0.13	0.12	0.04	0.06	0.09	0.03	
Ce	17.8	17.8	3.6	18.3	26.5	18.2	3.6	4.6	109.0	47.0	
Pr	0.6	0.6	0.001	0.6	0.6	0.2	0.01	0.01	0.1	0.1	
Nd	10.0	8.9	0.2	8.1	9.7	3.0	0.3	0.6	2.7	1.2	
Sm	14.7	16.0	0.5	13.3	14.8	4.3	0.8	0.8	4.55	2.0	
Eu	1.2	1.3	0.2	0.8	1.3	0.4	0.1	0.1	1.9	0.3	
Gd	72.0	75.6	2.7	52.6	79.9	23.9	3	3.6	27	14	4300
Tb	25.1	28.5	1.0	20.3	29.2	8.4	2.7	3.3	4	8	250
Dy	290.7	327.4	14.6	221.5	364	113.3	32.3	34.8	89	43	18000
Ho	102.9	115.6	6.2	77.9	132	42.4	13.5	14.1	32	13	3200
Er	427.8	474.9	30.5	340.0	589.9	199.2	69.6	74.1	144	62	31000
Tm	79.9	89.4	7.7	65.3	112	41.8	16.1	17.5	31	11	5000
Yb	634.7	721.3	76.7	540.6	843.2	338.6	156	164	248	82	43000
Lu	115.6	129.5	19.5	102.0	169.7	71.1	33.4	34.1	44	13	5700
Hf	7350	7282	11544	7730	9642	10773			9722	11711	4600
Th	97	113	23	111	137	48	27	39	518	301	
U	138	152	83	133	241	94	193	163	464	104	
Th/U	0.70	0.74	0.28	0.83	0.57	0.51	0.14	0.24	1.12	2.89	
ΣREE	1793	2007	163	1461	2373	865	331	352	737	297	110450

Notes: TE#: trace element SIMS pit number, see Figure 8. References (1) Strickland unpd; (2) Bouvier et al. 2011; (3) this study; (4) Cavosie et al. 2006.

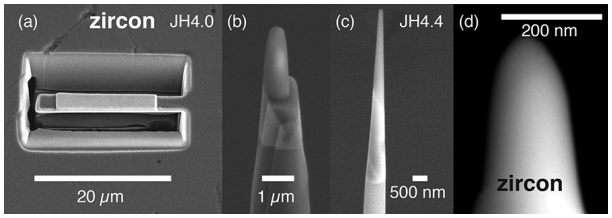

FIGURE 2. Milling of needle-shaped specimens of zircon for APT by focused ion bean (FIB). (**a**) FIB lift-out from polished surface of JH4.0. (**b**) Roughly milled tip. (**c** and **d**) Sharpened tips with radius of curvature <100 nm.

1500 nm (Figs. 2c and 2d). The orientation of each needle is normal to, and pointing toward, the polished surface.

The local-electrode atom probe (LEAP) instrument is described in detail elsewhere (Larson et al. 2013a; Kelly and Larson 2012; Gault et al. 2012). Analysis capabilities and protocols differ for electrically conducting vs. insulating materials. Analysis of insulators has recently become practical by development of commercial laser-stimulated ionization (Kellogg and Tsong 1980; Gault et al. 2006; Bunton et al. 2007; Larson et al. 2008). Insulating specimens are cooled to ~50 K at high vacuum and a high voltage (typically 4–14 kV) is applied (Fig. 3a). In this study, a pulsed UV laser (355 nm wavelength, pulse energy 400

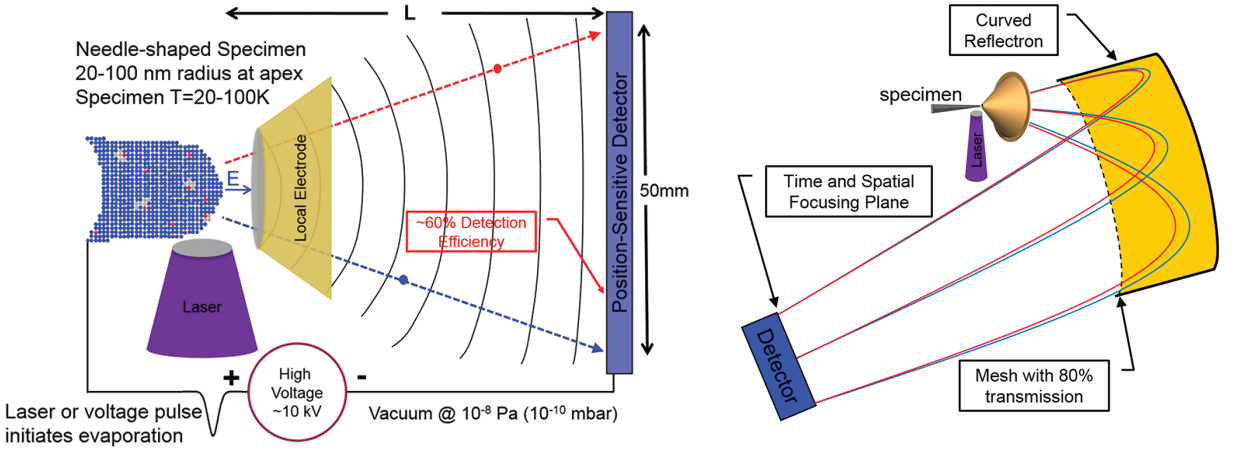

FIGURE 3. (**a**) Schematic drawing of the CAMECA local-electrode atom probe (LEAP) instrument. (**b**) Schematic of the LEAP 4000HR instrument used in this study with a curved reflectron to enhance mass-resolving power.

pJ, 200 kHz repetition rate) was focused on the specimen (2.5 μm diameter spot) to promote field evaporation of, on average, ~0.008 ions/pulse. Ions travel through vacuum toward the detector, yielding a time-of-flight measurement that is used to determine mass/charge. The LEAP 4000X HR incorporates a curved reflectron compensator (Panayi 2012) (Fig. 3b), which improves the mass resolving power to about 1000 (M/ΔM, FWHM) at the $^{28}Si^{+}$ peak while retaining the field of view of about 150 nm. For the specimens used in this study (~100 nm diameter at tip, radius of curvature <100 nm; Fig. 2d), the spatial resolution of detected atoms is about ±0.3 nm in X-Y-Z coordinates. From 10^7 to 4×10^8 ions were detected per specimen at rates of ~10^7 ions/hour. In principle, all ions are detected with an equal efficiency of ~37%. The ion detection efficiency is determined by the 60% detection efficiency of the microchannel plates times the 80% transmission of the mesh on both entrance and exit of the reflectron. The minimum detection limit is ~10 ppma (parts per million of atoms) per peak for these data, but the limited volume of the analysis and molecular interferences can limit detection. Spectra must be individually evaluated as some elements form ionized molecules, and some peaks have isobaric interferences.

Composition determinations

Composition is determined in atom probe tomography as follows. For microchannel plate detectors, the ion detection probability is known to be uniform with mass up to about 500 Da so all ions are assumed to have the same detection probability. A range is defined in the mass spectrum to denote the start and end of a given peak. The counts within this range are defined as the raw counts. The background counts are determined by examining the level of the spectrum on either side of the range and estimating the background contribution in the range by interpolation. The net signal counts are thus raw counts minus background counts. The composition of any volume in the three-dimensional image is determined simply from the sum of all the atoms in that volume.

Identification of peaks in the mass spectrum is straightforward when the peaks are isolated, although a multiplicity of peaks can be generated for an element. Each of the possible charge states is considered for any given isotope. Molecular ions occur in field evaporation and can be altered by the presence of the high electric fields on the specimen (e.g., H_3O^+ is a common ion). Hydrides of almost any element can form which complicates analyses for some specimens as discussed below.

When peak overlaps occur, a peak decomposition approach is used in the Integrated Visualization and Analysis System software (IVAS; Kunicki et al. 2006). For a mass spectrum for any given sub volume, this approach computes the probability that the peak may have contributions from neighboring peaks. For stable isotopes, this probability is based on average terrestrial isotope ratios. These ratios do not apply to radiogenic isotopes such as Pb. For Pb, we relied on the mass position, the concentrations of parent isotopes, and reasonable ages as discussed below.

It is not possible to correct for background in the ion maps or tomography as each datum may be signal or background. Only in collective measurements such as composition determinations from a volume can the background be subtracted. One can take the ratio of signal to background for some peak and note that statistically, any given datum will have this probability of being a signal event.

The sources of background events are manifold: (1) residual gas in the vacuum chamber can adsorb on the specimen and become ionized; (2) delayed evaporation of ions after pulses will not be timed correctly and contribute to the background continuum; (3) electronic noise in the detector; (4) dissociation of a molecular ion during acceleration into one charged and one uncharged entity can lead to untimed events; and even (5) cosmic rays may excite the detector. Most of these sources of background are low as evidenced by the high signal-to-noise ratio in general for APT. When analyzing a new type of material, data-collection conditions are first established to minimize out-of-time evaporation. This test is made before any data are quantified.

For any type of specimen, peak/background may be optimized. The following factors tend to improve background levels: high-pulse rate, lower-temperature, high-detection rate, high-pulse fraction (voltage pulse mode only), optimal laser pulse conditions (focus, spot size, alignment of laser), optimal laser pulse energy, and specimen surface (shape, absorbance of laser energy, thermal diffusivity, band gap) (see, Larson et al. 2013a).

The uncertainty in composition is computed from the square root of the sum of raw plus background counts. The range for peak integration and settings for background measurement are set visually from an expanded view of the spectrum. Since the binning peak size has an error uncertainty, the measurement is performed five times and the errors are added in quadrature.

The detection sensitivity of the APT technique (Larson et al. 2013a) can be assessed from the number of background counts in a range. Using the definitions of Currie (1968) for detectability, the net counts of a peak of interest that must be present in the spectrum to avoid being obscured by the background is calculated from 4.65 times the square root of the background. If the net counts are greater than that number, then the peak should be above background 95% of the time. The detection limit for any particular isotope is thus diminished if the corresponding peak resides on the delay tail of another peak. Clustering of low-concentration elements improves the detectability if the clusters can be isolated as is the case in this work.

Constructing the three-dimensional image

Constructing a three-dimensional image from the raw data requires converting an X,Y hit position on the detector to an x,y,z position of the atom in real space within the sample. This process is called reconstruction; for a review see Larson et al. (2013a, 2013b). Detector hits are first back projected onto a curved surface that represents the specimen surface. The sequence of hits on the detector corresponds to the sequence in which the atoms are back projected and this creates the third dimension of an image. A projection law must be used to back project each atom. The projection law is determined by the shape of the specimen apex, which is not perfectly known in today's instruments. To first order, the needle-shaped specimen can be modeled as a cone with a spherical endcap for which a projection can be modeled analytically. Note however, that though the relative position of atoms may be determined by this procedure, absolute positioning, i.e., accurate spatial scaling, is not achieved without additional information. A physical parameter such as atomic density or the specimen apex radius is used to fix the scaling.

Furthermore, because the specimen does not possess a perfect spherical endform, the reconstruction will contain errors whose local magnitude depends on the local deviation of the endcap from a spherical geometry (Larson et al. 2011).

In amorphous materials, the endcap can be smooth and approximately spherical though not tangential to the cone. In this case, the spherical approximation, with accounting for a non-tangential cap on cone, is good. For single-phase crystalline materials, low-index poles usually form small facets on the surface because atoms will not evaporate from the middle of a close-packed plane, but rather, the atoms on the edges of planes evaporate and the plane shrinks from its edges. These facets cause local deviations from a spherical surface and the ion trajectories from the center of poles are modified as a result. Lateral spatial resolution in metals between poles has been shown to be 100–200 pm (Kelly et al. 2009; Gault et al. 2009). Thus, although very high-spatial resolution is achieved in most images, it is not necessarily achieved in all locations of the image. Minerals generally do not show this tendency to form obvious facets, which means that the spatial resolution should be more uniform throughout the image.

In multiphase specimens, the surface can develop topography due to differences in the evaporation fields of the different phases. That is, if a small phase requires a high-electric field to evaporate relative to its surrounding matrix, then it will tend to protrude further into the high-electric field region before evaporating. Thus differential evaporation leads to a protrusion of the high-field material, which alters the trajectories of the ions toward the detector (Larson et al. 2013a, 2013b). The simple spherical-projection reconstructions that are prevalent today do not account for these protrusions and the spatial resolution locally can be several nm for a large evaporation field difference and a large size of the second phase. In the limiting case of a very small evaporation field difference, this trajectory aberration is minimized.

Methods for identifying clusters (nanometer-scale concentrations of one or more element) in atom-probe data have been the subject of various approaches (Blavette et al. 1988; Vurpillot et al. 2004; Miller and Kenik 2004; Miller et al. 2007; De Geuser et al. 2006; Cerezo and Davin 2007; Marquis and Hyde 2010; Stephenson et al. 2011; Serizawa and Miller 2013). The full details of these approaches are beyond the scope of this paper. Essentially, the local environment of any given solute atom in a data set is assessed for the presence of other solute atoms based on either spatial proximity or local composition. For local composition, a distribution is initially calculated by binning the data into small blocks containing a few hundred atoms per bin and then comparing the resulting distribution to one that would be obtained were the data random (Miller et al. 1996). For example, in the case of a random alloy containing two elements, the result would reflect a binomial distribution and any statistically significant deviation from this distribution would suggest clustering or partitioning in the data.

Cluster detection based on spatial proximity usually employs an algorithm known as "friends of friends" (Hyde and English 2000). In this method and its variants, geometric rules have been developed to associate atoms with a cluster if they are within a certain maximum distance of any other solute atom in the cluster. Alternatively, since the local composition can be computed at any point in the image, isoconcentration surfaces can be contoured in three dimensions throughout the data. These surfaces surround volumes of high solute content in the case of small precipitates or clusters. Given the relatively large nature of the clusters in this paper, we have found this latter approach to give the most straightforward interpretation of the clusters.

The isoconcentration method imposes a three-dimensional grid of points onto the data (following the method of Hellman et al. 2003) and then calculates the resulting concentration values at each grid point. This calculation is governed by two variables called voxel size and delocalization (O'Neill et al. 2006). Other variables that may have a substantial effect on the results of this method are the range definitions in mass spectra and the elemental concentration level chosen for the isoconcentration surface. As is the case with the friends-of-friends methods, it may be necessary to vary the input parameters of the isoconcentration technique to optimize the cluster identification as a function of the objective of the analyses and/or as the nature of the clusters themselves (Hyde et al. 2011).

In the current work, we have determined composition inside the clusters using a 3 at% Y surface in JH4.4 and a 0.5 at% Y surface in ARG2.5. The same 0.5 at% Y surface was used in ARG2.5 to remove the clusters from the data and calculate the surrounding zircon matrix composition. To extract the clusters and calculate the composition of the zircon matrix in JH4.4, however, we used a 1 at% Y surface (mainly due to the presence of substantial Pb in the matrix). This approach excludes a small zone at the cluster surface but minimizes the variability of the cluster compositions.

The mass resolving power (MRP) in time-of-flight spectroscopy depends on the ion flight time since MRP = $m/\Delta m = t/\Delta t$ (m = mass, t = time of flight, and Δt = time of departure spread) and Δt should be independent of flight time for laser pulsing. For this reason, the mass at which the MRP is measured should be stated. It is preferred to cite MRP values measured at mass/charge (m/n) ~30. In this work, there is a strong peak at m/n = 32, which corresponds to $^{16}O_2^+$. The MRP measured on this peak ranged between 900 and 1100 (FWHM) for all of this work.

Non-metamict zircon is a well-behaved material in an atom probe. It has high values of thermal diffusivity, which promote high cooling rates and therefore high-mass-resolving power in laser pulsing. It can withstand high hydrostatic stress (the stress in the specimen varies as the square of electric field which is very high). The fact that zircon field evaporates well is a sign that it has a high strength relative to its average evaporation field.

Molecular species and isobaric interferences in APT spectra

Molecular species and isobaric interferences are common in atom probe spectra, which can lead to sample-specific artifacts. Failure to identify such species can lead to erroneous concentrations. For instance, the trace element Ti, which is of interest for zircon thermometry (Watson et al. 2006), cannot be analyzed accurately due to $^{96}Zr^{2+}$ that overlaps $^{48}Ti^+$, the most abundant Ti isotope. More generally, hydride interferences are common and can cause elevated counts for peaks at mass, m+1 (and corresponding diminished peak counts at m). Hydrides are especially problematic for measurement of isotope ratios if the

higher mass peak at m+1 is at lower abundance, as is the case for the commonly analyzed stable isotope ratios of H, C, N, O, Mg, Si, Cl, S, Ca, and Cr. Heck et al. (2014) report special care in measuring carbon isotope ratios from pre-solar nanodiamonds by APT, which show an unexplained instrumental bias and anomalously high-measured levels of ^{13}C that may result from an isobaric interference on ^{13}C or deadtime corrections for ^{12}C. The hydride interference at 13 Da is especially challenging in nanodiamonds because $^{13}C/^{12}C$ ratios average 0.015 and significant amounts of H can reside in the specimen on the unavoidable grain boundaries.

Zircon is nominally anhydrous when fully crystalline, however, H is always present at some level, and water content typically increases with radiation damage and can exceed 10 wt% in metamict zircons (Aines and Rossman 1986; Nasdala et al. 2001a, 2003; Zhang et al. 2002; Geisler et al. 2003; Utsunomiya et al. 2007). In this study, crystalline domains of zircon were selected based on CL zoning, concordant U-Pb ages, and REE patterns, and verified by EBSD in the case of grain JH4.4. The current protocol for oxygen 2-isotope analysis at WiscSIMS is to tune mass 17 to ^{16}OH, which provides a monitor of H in each spot analyzed (Wang et al. 2014). However, this procedure was not yet developed when $\delta^{18}O$ was analyzed in the zircons of this study. Hydride interferences are evaluated for several adjacent peak positions in the APT spectra and their importance is found

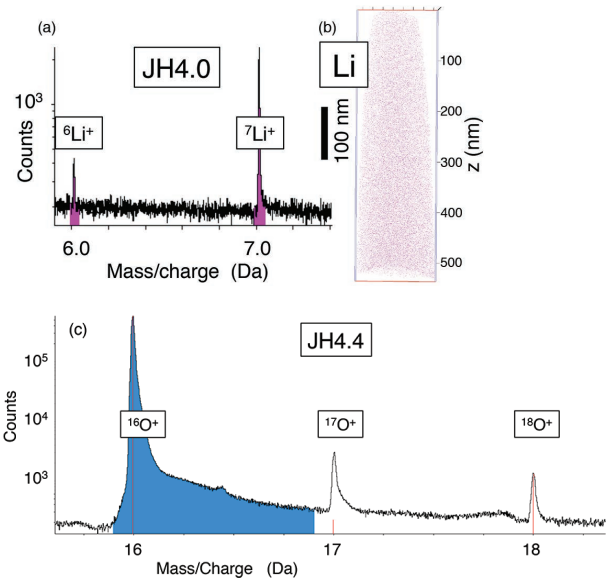

Figure 5. (**a**) APT mass spectrum at 6–7 Da showing peaks for Li in JH4.0. (**b**) Projection of atoms for Li in a needle-shaped 500 nm long specimen of JH4.0. (**c**) Mass spectrum at 16–18 Da showing peaks for three isotopes of oxygen and hydrides in JH4.4, see text.

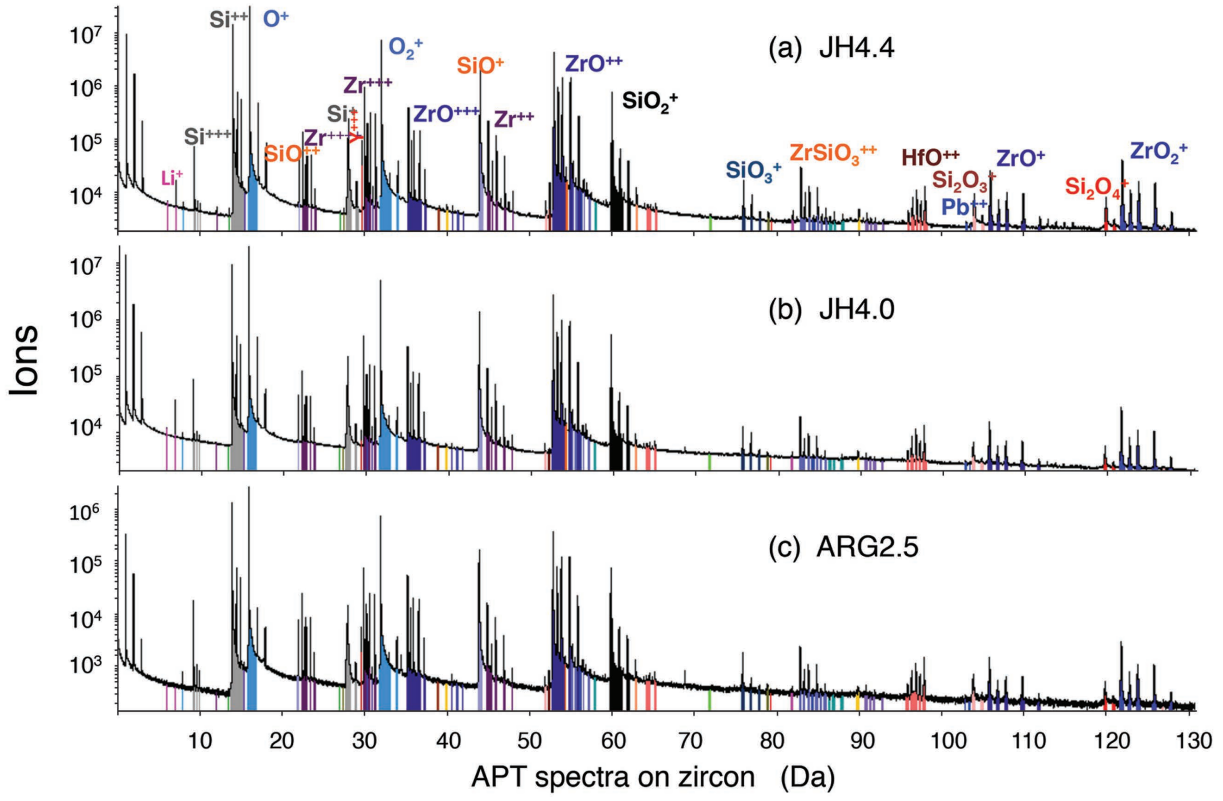

Figure 4. APT mass spectra from 1 to 130 Da for the three zircons of this study. (**a**) JH4.4. (**b**) JH4.0. (**c**) ARG2.5. Many elements form molecules and have multiple charge states, see text.

to be highly variable according to the element and proportions involved. The intensity of hydride interferences is significantly reduced for doubly ionized species (Tsong et al. 1983; Heck et al. 2014) and thus for this study, we consider it unlikely that the intensity of $(^{206}PbH)^{++}$ interference on $^{207}Pb^{++}$ is significant for the range of $^{207}Pb/^{206}Pb$ ratios measured (0.17 to 1.2) and the analytical precision reported (±4–17%).

Hydrogen is readily detected in an atom probe and all spectra have prominent H peaks at 1–3 Da (Fig. 4). A key question is the origin of the hydrogen. The detected hydrogen may come from the vacuum chamber volume, from the specimen itself, or both. Because hydrogen is difficult to remove from an ultrahigh vacuum, it is always a major component of the residual gas in an atom-probe system. The level of residual hydrogen can depend on previous samples, the length of time since venting, and the general system vacuum. If hydrogen mapping and quantification are to be performed in an atom probe, a careful effort must be made to distinguish its source. Hydrogen may appear in spectra as a monatomic ion (H^+), as molecular ions (H_2^+ and H_3^+), or as a hydride of other elements in the material.

Li and O by APT

Values of [Li] vary from 6 to 24 ppmw in the core of JH4.4 and 45 to 56 ppmw in the mantle of JH4.0 (Table 1). These concentrations are seen as clear peaks for both ^7Li and ^6Li (Figs. 4a, 4b, and 5a). The effect of hydrides on accuracy of values of δ^7Li has not been evaluated, although it is smaller than for most light stable isotopes because the lighter mass (^6Li) is less abundant. Counting statistics are a larger problem; isotope ratios cannot be measured by APT at sub-10‰ levels for a trace element. APT uniquely shows the distribution of individual atoms of Li (Fig. 5b), but SIMS is the preferred technique for analyzing trace element concentration or isotope ratio.

We tested the importance of hydride interferences for singly ionized adjacent oxygen peaks at 16–18 Da (Fig. 5c). No correction for hydrides was attempted. The apparent values of $\delta^{18}O$ mostly range from 100 to 400‰ higher than the true value for each zircon. The largest discrepancies are seen for the specimens with the highest $^1H/^{16}O$ ratios. These differences are interpreted to result from isobaric interferences at 18 Da from $^1H_2{}^{16}O$, $^{17}O^1H$, and $^{16}O^2H$. These isobars are cleanly separated from the ^{18}O peak at MRP = 2500 by SIMS (see Fig. 2 of Valley and Graham 1991; Kita et al. 2009), however the hydrides are not resolved at MRP ~1000 by APT, causing elevated ratios of the 18 Da/16 Da peak ratio (Fig. 5c). The hydride interference of $^1H^{16}O$ on ^{17}O can only be resolved by SIMS at MRP = 5000 (Kita et al. 2009) and the effect for measurements by APT is very large due to the low concentration of ^{17}O. Thus SIMS is preferred over APT for accurate analysis of oxygen isotope ratios at natural abundance levels.

Pb isotope ratios by APT

The APT spectra for each zircon shows peaks for doubly ionized $^{206}Pb^{2+}$, $^{207}Pb^{2+}$, and $^{208}Pb^{2+}$ at 103, 103.5, and 104 Da, respectively (Fig. 6). No singly ionized Pb^+ is detected at 204–208 Da. The non-radiogenic isotope, ^{204}Pb, was not detected, consistent with SIMS data that show low $^{204}Pb/^{206}Pb$ ($<1 \times 10^{-4}$, $<9 \times 10^{-5}$, and $<6 \times 10^{-6}$ for JH4.4, JH4.0, and ARG2.5, respectively). There are no apparent interferences for peaks at 103 and 103.5 Da (^{206}Pb and ^{207}Pb). A small contribution of ^{206}PbH for ^{207}Pb cannot be ruled out, but as discussed above under Molecular Species it is less than the reported uncertainty (3–7%) and probably less than 1% of the ^{207}Pb peak. The peak for $^{208}Pb^{2+}$ at 104 Da, however, includes a large isobaric interference by $^{28}Si_2^{16}O_3^+$ that cannot be resolved at MRP = 1000. The identification of this peak is verified for ARG2.5 (Fig. 6) where all of the detectable Pb is in clusters. For atoms located within the clusters, there are three Pb peaks, but the peak at 104 is disproportionately high compared to SIMS data that show $^{208}Pb/^{206}Pb = 0.095$, indicating that much of the 104 Da peak in the APT data are not from ^{208}Pb (Fig. 6a). Outside of clusters, there are no detectable peaks at 103 and 103.5 Da showing that there is no Pb and thus the peak at 104 Da is Pb-free (Fig. 6b). The series of peaks seen for Si, SiO, and SiO_2, suggest that Si_2O_3 will be present at 104 Da and this is confirmed by the small peak at 105 Da in Figure 6b, which is ~5% as intense as 104,

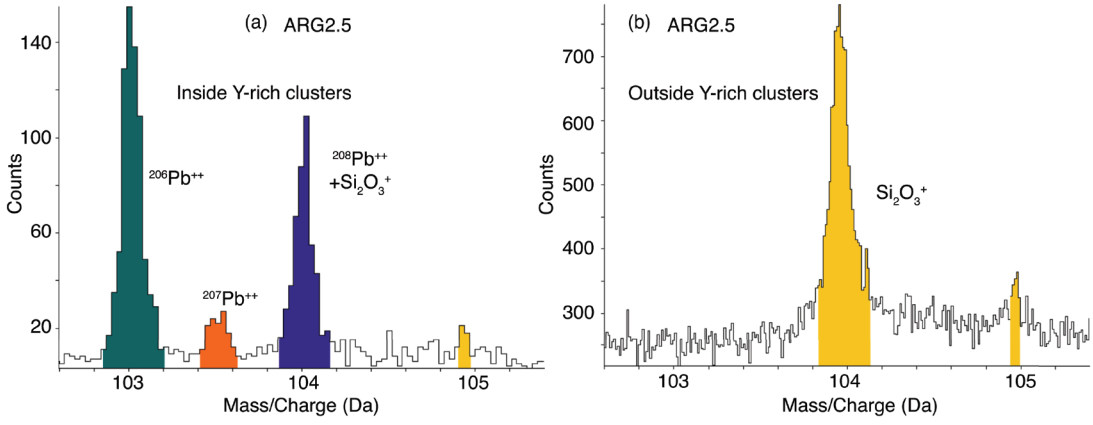

FIGURE 6. APT mass spectra from 103–105 Da in zircon ARG2.5. (**a**) Spectra for ions coming from volumes within clusters. (**b**) Spectra for ions from outside of clusters. Peaks at 103 and 103.5 Da are $^{206}Pb^{++}$ and $^{207}Pb^{++}$, respectively. The peak at 104 Da is $^{208}Pb^{++}$ and $^{28}Si_2^{16}O_3^+$ inside of clusters and $Si_2O_3^+$ only for outside of clusters, where there is no measureable Pb. The peak at 105 Da is singly substituted (^{29}Si and ^{17}O) $Si_2O_3^+$.

consistent with singly substituted ^{29}Si and ^{17}O in Si_2O_3 (natural abundances are: $^{29}Si/^{28}Si$ ~0.050 and $^{17}O/^{16}O$ ~ 0.00038). Thus for all of the zircons in this study, ratios of $^{207}Pb/^{206}Pb$ can be measured either for entire specimens or for sub-domains such as clusters. The concentration of ^{208}Pb cannot be deconvoluted from its interference in zircon, but this might be possible in Si-free minerals such as monazite (Snoeyenbos et al. 2012), xenotime, apatite, baddeleyite, or rutile.

Samples

Three zircons were selected for study by APT based on earlier SEM and SIMS studies. The analyzed domains range in age from 4.4 to 2.5 Ga. The sample numbers of these three zircons have been simplified from those reported in earlier papers to designate locality and age. The abbreviated and full names are: JH4.4 = 01JH36-69, JH4.0 = 01JH13b/2.5M/8-4, and ARG2.5 = ARG05-28-2. The oldest zircon, JH4.4, has been examined in the most detail and provides the best comparison of data from SIMS and APT. The other two samples illustrate similarities and differences, and provide additional support for interpretations of the APT results.

JH4.4

JH4.4 is a detrital zircon (01JH36-69), recovered by electric pulse disaggregation of quartzite (sample 01JH36) from the Jack Hills, which are in the Narryer belt of the Yilgarn craton, Western Australia. The locality is midway between the East and West Traverses of Cavosie et al. (2004) and is ~1 km NE of Eranandoo Hill on the West Traverse where the first 4.3 Ga (Compston and Pidgeon 1986) and 4.4 Ga (Wilde et al. 2001) zircons from Earth were found. This quartzite rock is a metamorphosed sandstone as evidenced by dark bands of detrital minerals, dominantly chromite and zircon (minor rutile), that outline flattened cross-beds (Fig. 7a). The rock also contains minor metamorphic chromian-muscovite, tourmaline and monazite. Whole-rock analysis by XRF yields 96.9 wt% SiO_2; minor Al and K (white mica); Cr (mica and chromite); and 87 ppmw Zr (detrital zircon) (Cavosie et al. 2004).

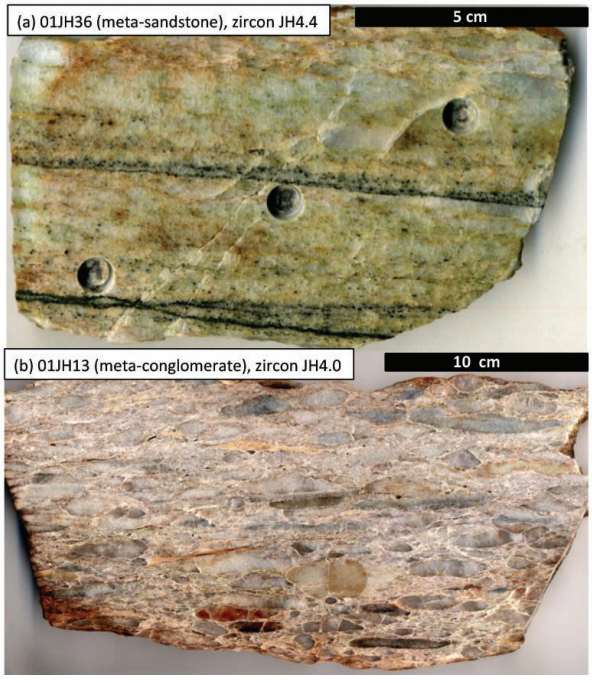

Figure 7. Photographs of polished rock surfaces from Jack Hills, Western Australia. (**a**) Meta-sandstone sample 01JH36 from which zircon JH4.4 was separated. (**b**) Meta-conglomerate sample 01JH13 from which zircon JH4.0 was separated.

Because of its large size (230 × 230 × 430 μm) and old age (4.4 Ga, Cavosie et al. 2007; Valley et al. 2014a), zircon JH4.4 was ground, repolished, and studied 4 times. The first two surfaces were ground shallowly so as not to remove smaller zircons in the same mount. As a result, surfaces 1 and 2 (Cavosie et al. 2004, 2005, 2006) did not penetrate the core of the crystal, and only exposed the wide younger overgrowth; CL images of surfaces 1 and 2 showing analysis spots and patchy CL patterns are published in those papers. Eleven SIMS analyses of age were made on surface 1 with the oldest spot in the core yielding 85% concordance and a $^{207}Pb/^{206}Pb$ age of 4324 ± 18 Ma (Cavosie et al. 2004). One analysis of the overgrowth at the crystal termination yielded a discordant 3.4 Ga age. Surface 2 was analyzed for $\delta^{18}O$ five times, but only one pit ($\delta^{18}O$ = 4.6‰) in the core was interpreted as normal in appearance by SEM; others were rejected as irregular by criteria described by Cavosie et al. (2005). The rejected values average 4.6‰ in the core and 6.2‰ in the rim. REEs were measured twice on surface 2 (Table 1; Cavosie et al. 2006).

JH4.4 was subsequently deeply ground to approximately its mid-section and repolished, sequentially exposing surfaces 3 and 4 that were less than a few micrometers apart. These surfaces were imaged by SEM (CL, SE, BSE, EBSD) (Figs. 8a–8c), and analyzed by SIMS in 10 to 20 μm diameter spots to determine age, oxygen two- and three-isotope ratios, and trace element compositions. CL patterns of surfaces 3 and 4 reveal the crystal's core, which shows distinct concentric zoning (Fig. 8a). Surfaces 3 and 4 are the topic of this study and are interpreted to preserve the early Hadean history of the grain (Valley et al. 2014a). Age was measured six times on surface 3 (Cavosie et al. 2007; Valley et al. 2014a); pit locations are shown with blue circles in the SE image of surface 4 (Fig. 8c). All three analyses of the core yield concordant overlapping U-Pb ages with an average $^{207}Pb/^{206}Pb$ age of 4374 ± 6 Ma (Figs. 8c and 9a; Table 2). Three analyses of the outer rim, where it is ~30 μm thick, yield minor discordance and $^{207}Pb/^{206}Pb$ ages averaging 3400 Ma (Figs. 8c and 9a; Table 2). This rim age correlates to the intrusive age of the Dugel orthogneiss, which crops out adjacent to the Jack Hills (3.38–3.35 Ga; Kinny and Nutman 1996; Pidgeon and Wilde 1998; Cavosie et al. 2004), but a more distant source cannot be ruled out for this zircon.

The CL image of surface 4 shows more than one episode of dissolution and growth as is typical in igneous zircons. The innermost core (~100 × 200 μm) is off-center and truncated by subsequent layers. The "mantle" of this grain (between the core and rim) shows concordant zoning that is locally cut by irregular disturbed domains that are dark and featureless in CL. The disturbed domains [D in Fig. 8a] show ~20% weaker diffraction by EBSD suggesting that they experienced radiation damage (Valley et al. 2014a). The largest and most prominent disturbed domain measures ~30 × 150 μm. Surfaces 1 and 2 of this zircon expose the mantle region and the CL image shows multiple disturbed

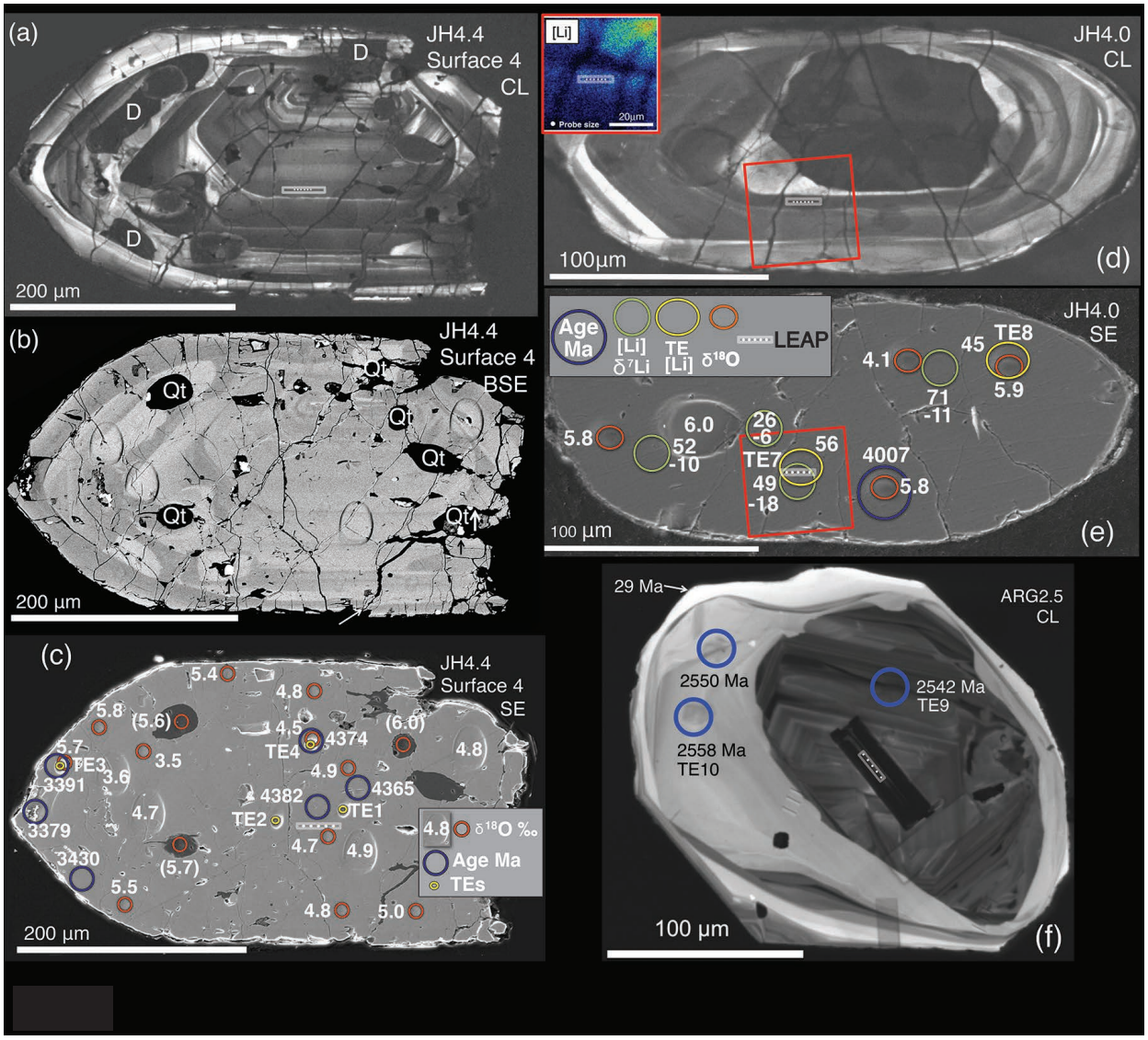

Figure 8. SEM images of the three zircons in this study. (**a**) CL image of surface 4 in JH4.4 showing concentric banding of the core and a 10–30 µm rim. The white rectangle near the center of the grain is the location of the FIB lift-out for APT specimens. D marks disturbed domains. (**b**) BSE image of surface 4 in JH4.4 showing inclusions of quartz (black) and xenotime (bright, up arrows). Brighter bands contain more REEs, Y, U, Th, and Pb. Four large 20 × 30 µm SIMS pits were for oxygen 3 isotopes. (**c**) Composite BSE-SE image of surface 4 of JH4.4 showing the locations of all SIMS measurements on surfaces 3 and 4. (**d** and **e**) CL and SE images of JH4.0 showing concentric banding, a dark disturbed core and the locations of SIMS analysis pits. The inset in **d** shows a scanning ion image of [Li] from the area around the APT sample locality; brighter colors are Li-richer. (**f**) CL image of ARG2.5 showing concentric zoning and the location of SIMS pits and APT specimens.

domains that may have compromised the earlier data (Fig. 1a in Cavosie et al. 2006). The outer rim of zircon JH4.4 is 10–30 µm thick, cuts the earlier growth bands and disturbed domains, and preserves fine-scale zoning, suggesting an igneous origin. The outer form of this crystal is subhedral showing gentle (relative to some JH zircons) rounding from sedimentary transport. This zircon is broken at one end, despite using electric pulse disaggregation, a relatively gentle, non-compressive method for disaggregating the host quartzite that yields fewer broken zircon fragments (Cavosie et al. 2004).

The BSE image of surface 4 (Fig. 8b) shows that most of the grain is zircon with subtle compositional zoning that correlates to CL. As is common in zircon, dark bands by CL are enriched in U, Th, Pb, Y, and REEs causing them to be brighter by BSE. The disturbed domains are also bright in BSE, suggesting that they are likewise enriched in these elements. The prominent mineral inclusions are quartz, which is black in BSE (Fig. 8b) because the gain of the detector was adjusted to discriminate small differences within zircon. The largest rounded quartz inclusion measured 50 × 100 µm in surface 3, but is smaller in surface 4 (Fig. 8b). Xenotime inclusions are also identified by EDS (up arrows, bright BSE, bright CL). Several generations of fractures are seen including late

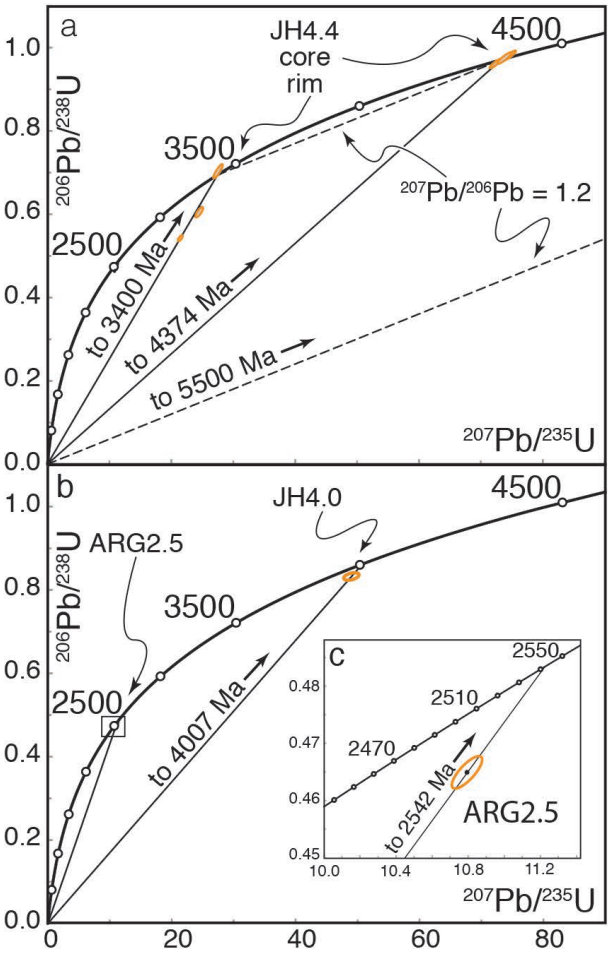

Figure 9. U-Pb concordia diagrams for three zircons. (**a**) Three analyses from the core of JH4.4 are concordant and overlap with an average age of 4374 ± 6 Ma. Three analyses on the rim yield a Pb-Pb age of 3400 Ma. The measured $^{207}Pb/^{206}Pb$ ratio of 1.2 from within clusters defines the slope shown by dashed lines. This is not interpreted as a conventional Pb/Pb age as projected from the origin (5500 Ma), but rather as the composition of Pb that was concentrated in clusters at 3400 Ma during reheating. (**b**) Nearly concordant analyses nearest to the APT specimens in JH4.0 and ARG2.5.

hairline fractures with no visible mineralization and earlier cracks filled with quartz. Some cracks displace growth bands seen by CL. The displacement of CL bands by quartz-filled cracks locally offsets banding in the outer edge of the crystal (arrow, bottom edge of Fig. 8b), showing that these features postdate sedimentary abrasion of the zircon grain and probably result from burial and metamorphism of the host sandstone.

Slight misorientations of zircon crystal structure are also shown by EBSD in the lower right (as shown in Figs. 8a–8c) portion of the crystal (up to 8°, Valley et al. 2014a). The main portion of the crystal, including the core, is oriented with the [100] axis normal to the polished surface and parallel to the long axis of APT specimens. The domains of differing orientation are sharply bounded by visible brittle fractures. Some fractures are healed by zircon that is dark in CL and crystallographically oriented relative to adjacent zircon. Other cracks appear unhealed and formed later.

JH4.0

JH4.0 is a detrital zircon (01JH13b/2.5M/8-4) from metaconglomerate (sample 01JH13) in the Jack Hills, Western Australia. This sample is from the same 2 m outcrop on Eranondoo Hill where samples W74 (Compston and Pidgeon 1986; Wilde et al. 2001) and 01JH-54 (Cavosie et al. 2004) were collected. The rock is a gray flattened-quartz-pebble metaconglomerate with accessory minerals including rutile, detrital zircon, and chromite, bright-green metamorphic chromian-muscovite and monazite (Fig. 7b). A whole-rock XRF analysis of sample 01JH54, from the same layer as 01JH13, shows 94.9 wt% SiO_2 and 318 ppmw Zr (Cavosie et al. 2004).

The CL image of JH4.0 (Fig. 8d) shows a dark disturbed core, a thin bright mantle that cuts both older and younger domains of the crystal and a concentrically zoned outer portion that is marked by multiple episodes of resorption and growth as is common in igneous zircons. There is no continuous rim forming a younger overgrowth as in JH4.4.

The $^{207}Pb/^{206}Pb$ age of zircon JH4.0 was measured from the concentrically zoned domain (Figs. 8d and 8e). The $^{207}Pb/^{206}Pb$ age is 4007 Ma and the U/Pb ages are 97% concordant (Fig. 9b) (Cavosie 2005).

The $\delta^{18}O$ values of three spots in the concentrically zoned domain of JH4.0 average 5.9 ± 0.2‰ (2 SD) (Ushikubo et al. 2008). One analysis of the disturbed core yielded an unreliable value of 4.1‰.

Table 2. Summary of SIMS data for U-Pb ages of zircons JH4.4, JH4.0, and ARG2.5

Spot	Grain area	U (ppm)	Th (ppm)	Th/U	$^{206}Pb^*/^{238}U$ age (Ma)	1σ err	$^{207}Pb^*/^{206}Pb$ age (Ma)	1σ err	$^{208}Pb^*/^{232}Th$ age (Ma)	1σ err	% conc.	Ref.
					ARG2.5 (ARG05-28-2)							
2.1	core	672	224	0.35	2462	9	2542	5			97	1,2
					JH4.0 (01JH13b-8-4)							
8.4.2	mantle	157	17	0.11	3904	21	4007	22			97	3
					JH4.4 (01JH36-69)							
1	core	140	92	0.66	4412	25	4382	5	4445	47	101	4
2	core	138	95	0.71	4349	24	4365	5	4374	52	100	4
3	core	93	66	0.74	4391	29	4374	6	4384	61	100	4
4	rim	61	16	0.27	3436	42	3379	13	3050	147	102	4
5	rim	119	189	1.64	2798	19	3391	12	492	26	83	4
6	rim	58	43	0.77	3053	32	3430	16	1206	62	89	4

Note: References: (1) Strickland pers. comm 2012; (2) Strickland et al. 2011; (3) Cavosie 2005; (4) Valley et al. 2014a.

ARG2.5

ARG2.5 is a xenocryst zircon (ARG05-28-2) from granodiorite of the Vipoint pluton in the Grouse Creek Mountains, northern Utah. The Vipoint pluton represents one of four plutonic suites emplaced into the lower plate of the Albion-Raft River-Grouse Creek metamorphic core complex between 32 and 25 Ma (Strickland et al. 2011a, 2011b). Zircons from sample ARG05-28 have igneous rims with average $^{206}Pb/^{238}U$ ages of 29.0 ± 0.3 Ma and inherited cores that range from 1990 to 2620 Ma. Monazite ages record sillimanite-grade metamorphism in wallrocks of the pluton synchronous with mid-crustal intrusion at ca. 32 to 27 Ma (Strickland et al. 2011a). These results indicate that in the Oligocene, zircon rims grew on Precambrian cores during a prolonged period of magmatic recycling and high-grade metamorphism in the mid-crust.

Zircon ARG2.5 has a core that is relatively dark by CL, but shows distinct concentric zoning in the domain dated at 2542 Ma by SIMS and where the FIB lift out was made for APT (Fig. 8f). The lower part of this dark core has more complex zoning and was not sampled. The outer margin of the core was resorbed and is overgrown by a medium-bright mantle, which is indistinguishable in age from the core (Figs. 8f and 9b) (Strickland et al. 2011a; Strickland, personal communication). The thin outermost rim is brightest in CL and correlated to overgrowths that were dated at 29 Ma in other zircons from this sample.

The $\delta^{18}O$ values of zircons from sample ARG05-28 average 5.3 ± 0.5‰ (rims) and 6.3 ± 0.5‰ (cores) (Strickland et al. 2011b). Five APT specimens were milled from a FIB lift-out in the core of the zircon near the 2542 Ma analysis spot (Valley et al. 2012).

Results

JH4.4

SIMS data. Oxygen isotope ratios were measured a total of 15 times in the zircon and three times in quartz inclusions on surface 4 of JH4.4. Four zircon analyses included all three stable isotopes of oxygen making prominent, large, ~20 × 30 × 2 µm pits (Figs. 8b and 8c). The oxygen three-isotope data plot along the terrestrial fractionation line (TFL) in excellent agreement with other Jack Hills zircons and zircons from Earth in general (Valley et al. 2007, 2014a; Fig. 10). The deviation from TFL

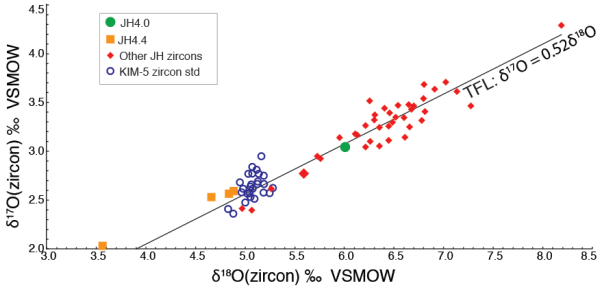

Figure 10. Oxygen three-isotope plot for Hadean zircons from the Jack Hills, including JH4.4 and JH4.0. All analyses fall within analytical uncertainty of the terrestrial fractionation line (TFL) as defined for bulk silicate Earth by mantle-derived zircons (blue). One spot on JH4.4 was of a disturbed domain (D) that yielded a lower $\delta^{18}O$, but still plots on TFL (data from Valley et al. 2014a).

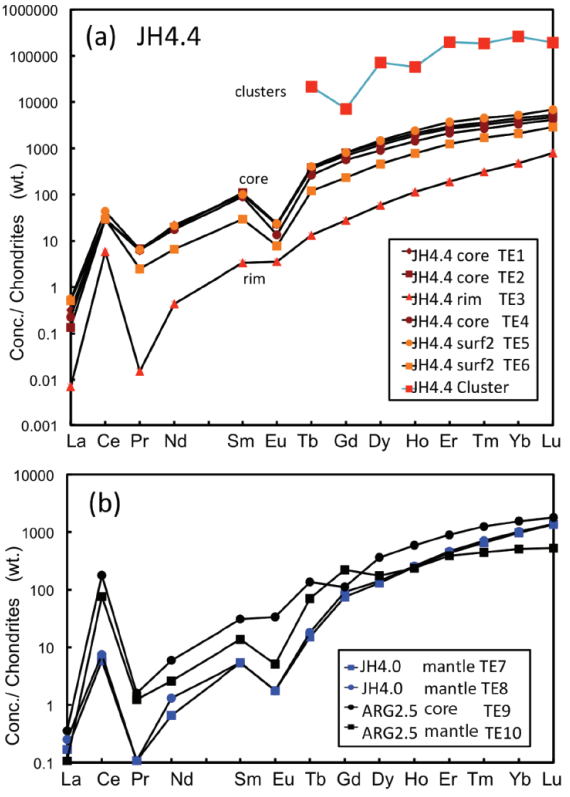

Figure 11. Chondrite-normalized plot of rare-earth elements (REEs) analyzed by SIMS. HREEs are also measured by APT from clusters in (**a**) JH4.4; (**b**) JH4.0 and ARG2.5.

($\Delta^{17}O = \delta^{17}O - 0.52\delta^{18}O$) is 0 ± 0.2‰, in excellent agreement with analyses of the KIM-5 zircon standard, which is a mantle megacryst from kimberlite (Page et al. 2007). Analysis of $^{18}O/^{16}O$ created smaller 10 µm pits (Fig. 8c). All analyses of the core and mantle except two that are in the dark disturbed zone average $\delta^{18}O$ = 4.8 ± 0.6‰. The four analyses of the zircon rim are distinctly higher, averaging $\delta^{18}O$ = 5.6 ± 0.5‰ (2 SD). The two analyses of disturbed zircon were made on different days in oxygen 3-isotope and oxygen 2-isotope mode and are in perfect agreement, but over 1‰ lower in $\delta^{18}O$ (3.5, 3.6‰). The $\delta^{18}O$ value of the disturbed domain is not reliable due to lack of an appropriate SIMS standard, and because the compositions may be altered.

The three SIMS analyses of quartz inclusions in zircon JH4.4 average $\delta^{18}O$ = 12.6 ± 0.4‰. For comparison, six analyses by laser fluorination of millimeter-size chips of the matrix quartz from the quartzite enclosing JH4.4 average $\delta^{18}O$ of 12.71 ± 0.08‰ (2 SD) (Cavosie et al. 2005, App. 4).

Trace elements were measured by SIMS twice on surface 2, and three times in the core, and once in the rim of surface 4. The 3.4 Ga rim of this zircon is distinctly different from the core; REE concentrations are an order of magnitude lower than the other five spots, the Ce anomaly is larger, and the Eu anomaly is smaller (TE3; Fig. 11a). The five REE analyses from the core and mantle of JH4.4 are similar with positive slopes and prominent positive Ce and negative Eu anomalies. Values of [Ti] range from 10.0 to 18.4 ppm in the core of JH4.4 and one analysis of

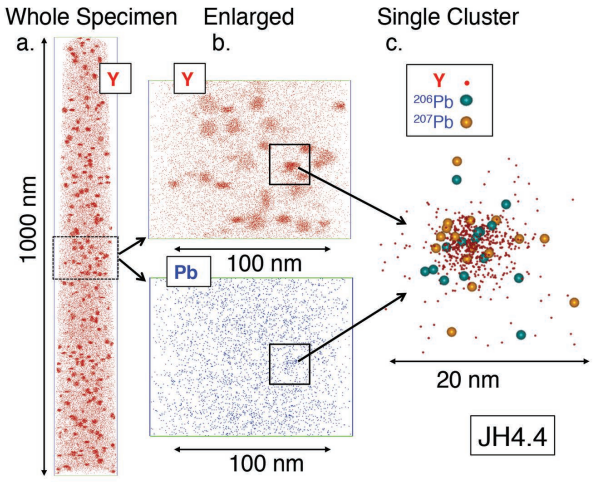

FIGURE 12. Atom probe tomography (APT) showing the distribution of Y and Pb atoms within a 1000 nm long needle-shaped specimen of JH4.4. (**a**) Y projected for the full volume of the specimen. The smallest orange spots are individual Y atoms; the larger orange domains are ~10 nm clusters of Y atoms. (**b**) Enlarged view showing clusters of Y atoms (top). Clusters of Pb are obscured because data are projected through the ~100 nm thick specimens (bottom). (**c**) Enlarged view of Y, ^{207}Pb, and ^{206}Pb in one cluster from **b**. These images can be viewed as rotating three-dimensional movies in the online Supplemental Material[1].

the rim is 2.5 ppm (Table 1).

APT data. Two needle-shaped specimens were milled from the core of JH4.4 using standard site-specific focused ion beam (FIB) methods to dimensions of ca. 100 × 100 × >1500 nm and analyzed by APT as discussed by Valley et al. (2014a). A total of 600 million ions were detected, 2×10^8 from specimen 1 and 4×10^8 from specimen 2. The elemental and isotopic compositions within these specimens are bimodal with small ~10 nm domains (clusters) concentrated in elements that are less compatible, or incompatible, within the crystal structure of zircon including Pb, Y, and REEs (Fig. 12). Concentrations of Y are as high as 8 at% in the centers of clusters and grade outward to lower values over ~5 nm (Fig. 13a). The location of clusters and their boundaries can be defined in various ways. In this sample, the contour for 3 at% Y is used to define the boundary of a cluster. The average Y content inside the 3 at% contours surrounding clusters is 4.4 at% (10.5 wt%). The sum of Y + REEs totals over 20 wt% within the clusters (Table 1). Pb and P are also concentrated inside of the clusters, but at lower levels of 4600 and 1600 ppmw, respectively. Li is not concentrated in clusters. Concentrations of Zr and Hf are correspondingly lower in the clusters.

There are 400 clusters in the total analyzed volume of two specimens (4.2×10^7 nm^3 = 0.04 µm^3) based on the 3 at% Y criteria, including 86 that are cut by the edges of the data for each specimen. There is approximately one cluster per 100 000 nm^3 of zircon in JH4.4. Most clusters are spaced 10–40 nm from their nearest neighboring cluster and the nearest-neighbor distances average 24.2 nm, center-to-center (Fig. 14).

The clusters are equant to flattened in shape. Two sets of clusters have preferred crystallographic orientations [flattened parallel to (100) and (010)] that are evident in the rotating tomographic movies for domains with Y > 3 at% (Appendix 1). Some of the smaller clusters appear more equant and are difficult to classify. A qualitative determination based visual examination of the clusters suggests that there are approximately equal numbers of each set, (100) and (010), and no consistent differences have been identified for chemistry.

The geometric shape of clusters can be affected by the choice of reconstruction variables in IVAS. However, any distortions will uniformly affect all clusters in the same way and every ef-

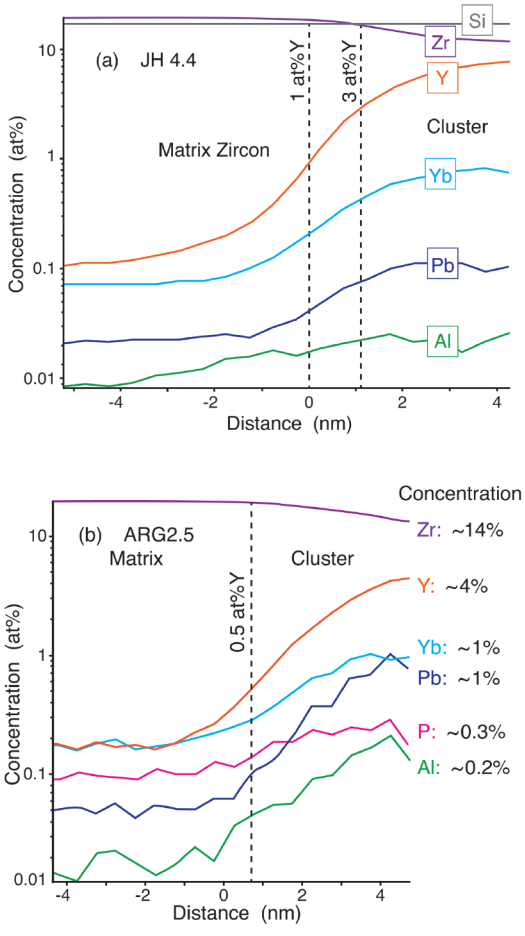

FIGURE 13. Radial distribution histograms of clusters in zircons JH4.4 (**a**) and ARG2.5 (**b**). The clusters in JH4.4 (**a**) contain up to 8 at% Y and higher concentrations of Pb, and HREE including Yb. For quantitative analysis and imaging of clusters, the volume inside clusters is defined by the contour of 3 at% Y, and the volume outside of clusters is set by <1 at% Y. In ARG2.5 (**b**), clusters contain up to 4 at% Y and 1 at% Pb with collocated concentrations of HREE, and smaller increases in P and Al. The volume inside of clusters is defined by the contour for 0.5 at% Y. [Zr] is less in both sets of clusters to compensate for increases of Pb, Y, and REEs.

[1] Deposit item AM-15-75134, Movies. Deposit items are stored on the MSA web site and available via the American Mineralogist Table of Contents. Find the article in the table of contents at GSW (ammin.geoscienceworld.org) or MSA (www.minsocam.org), and then click on the deposit link.

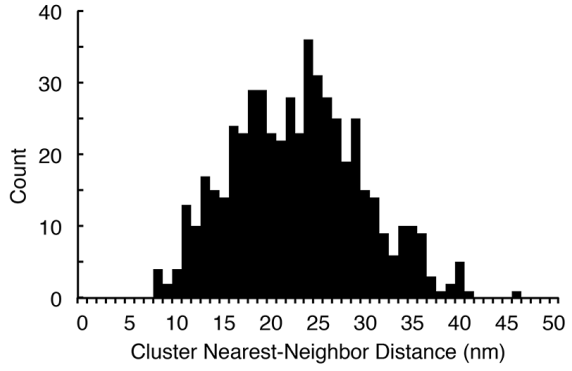

FIGURE 14. Histogram of the distances from the center of each cluster to the center of its nearest neighboring cluster in zircon JH4.4.

fort has been made to achieve accurate shape reconstructions. The fact that there are groups of clusters that are flattened in two different directions cannot be due to reconstruction artifacts and is thus considered to be real.

The two specimens of zircon JH4.4 yielded the largest data set of the three zircons that have been analyzed by APT (6×10^8 ions). A total of 15 591 atoms of ^{207}Pb and ^{206}Pb were detected after background correction (Table 3, not including the domains between the 1 and 3 at% Y contours). The signal/background ratio is 1.088 for ^{207}Pb and thus background correction is important. The ^{207}Pb/^{206}Pb ratio is 0.52 ± 0.04 for the entire data set. For the combined volume of 400 clusters (defined by the 3 at% Y contour), the ^{207}Pb/^{206}Pb ratio is 1.2 ± 0.05 and the ratio for outside of clusters (<1 at% Y) is 0.3 ± 0.05 (Table 3). The concentric shell between 1 and 3% represents a mixture and yields a ratio of ~1.15. Other contour intervals were investigated and there is no significant difference in the measured ^{207}Pb/^{206}Pb ratios.

JH4.0

SIMS data. Trace elements were measured twice by SIMS in the concentrically zoned domain of JH4.0 (Bouvier et al. 2012) and [Li] plus δ^7Li were measured four times including two analyses/each from the core and mantle (Ushikubo et al. 2008) (Fig. 8e). For analyses in the concentrically zoned domain, concentrations of Li are uniformly high (45 to 56 ppmw) and values of δ^7Li are low (–10 and –18‰). The specimens for APT analysis correlate most closely to REE analysis spot TE7 and are from a dark CL band that is rich in Li. Li was mapped across this domain by SIMS. Note that intensity is reversed in Figure 8d; brighter colors represent higher [Li] in the scanning ion image (inset) but zones that are enriched in Li, Y, REEs, U, and Th are darker by CL (Ushikubo et al. 2008). The REEs are identical in both spots that were analyzed for trace elements by SIMS. A chondrite-normalized diagram shows a positive slope, and prominent positive Ce and negative Eu anomalies (Fig. 11b; TE7 and TE8). Titanium varies from 6.1 to 7.7 ppm in these spots (Table 1).

APT data. APT specimens were obtained from the darkest undisturbed CL band of the concentrically zoned domain in JH4.0 (Fig. 8d) (Valley et al. 2012). Five specimens were analyzed by APT, yielding from 10 to 90 million ions each for a total of 2.15×10^8. Peaks are prominent for Zr, Si, ZrO_x, and SiO_x (Fig. 4b). Several trace elements were identified including Li, P, Y, Pb, Hf, and HREEs (heavy REEs). No zoning, heterogeneity, or clusters are seen for these elements (e.g., Figs. 5b and 15d). There were 6877 Pb ions detected with a ^{207}Pb/^{206}Pb ratio of 0.42 ± 0.07 (2 SD). Uncertainty of the Pb isotope ratio and for trace elements is larger than for the other zircons due to a low concentration of Pb, which is homogeneously dispersed within the specimens, causing a poor signal/background ratio (1.045 for ^{207}Pb).

There are no detectable spectral interferences for ^{6}Li$^+$ and ^{7}Li$^+$ (Fig. 5a). The measured concentration is 237 ppma (Table 1). The distribution of Li atoms within this specimen is uniform (Fig. 5b), which shows that elevated values of [Li] are not caused by defects or inclusions. These results support ionic substitution of Li in an interstitial site that charge balances trivalent Y and REEs (Ushikubo et al. 2008).

ARG2.5

SIMS data. Trace elements were measured twice by SIMS, once in the core and once in the mantle of ARG2.5 (TE9 and TE10; Figs. 8f and 11b). The REE patterns, like the ages, are similar for these two domains, showing a prominent positive Ce anomaly and flat HREEs. The negative Eu anomaly is muted for the core (TE9; Fig. 11b). Titanium varies from 12.9 to 16.8 ppm. Analysis TE9 is from the same domain as the APT sample.

TABLE 3. Ratios of ^{207}Pb/^{206}Pb measured by SIMS and APT in zircons JH4.4, JH4.0, and ARG2.5

Sample Region	^{207}Pb/^{206}Pb Age (Ma) SIMS	^{207}Pb/^{206}Pb SIMS	^{207}Pb/^{206}Pb APT	2 SD	^{206}Pb background corrected	^{207}Pb background corrected	^{206}Pb raw cts	^{206}Pb background	^{207}Pb raw cts	^{207}Pb background
ARG2.5 (ARG05-28-2)										
Full volume	2542 Ma	0.1684	0.17							
Within clusters (Y > 0.5 at%)			0.17	0.03	1135	191	1463	328	377	186
JH4.0 (01JH13b-8-4)										
Full volume	4007 Ma	0.4269	0.42	0.07	4837	2040	58200	53363	47222	45182
JH4.4 (01JH36-69)										
Full volume (core)			0.52	0.040	10255	5336	87734	77479	65728	60392
Core	4374 Ma	0.5472								
Rim	3400 Ma	0.2867								
Within clusters (core) (Y > 3 at%)			1.2	0.049	2345	2942	3431	1086	4421	1479
Outside clusters (core) (Y < 1 at%)			0.33	0.048	7439	2223	84607	77168	57271	55048

Notes: Background-corrected atoms of Pb detected and ^{207}Pb/^{206}Pb measured by APT. Pb-rich clusters concentrate Pb, Y, and REEs in ARG2.5 and JH4.4 and are defined based on Y concentration, see text.

APT data. Four specimens were milled from ARG2.5 and analyzed by APT. From 9 to 35 million ions were counted from each specimen for a total of 7×10^7 ions. There are prominent peaks for Zr, Si, ZrO_x, and SiO_x. Several trace elements were identified including P, Y, HREEs, Hf, and Pb. The concentrations of Y, REE, and Pb are strongly zoned in ARG2.5 and concentrated in clusters for all four specimens (Figs. 15a–15c).

The proximity histogram profile shows a radial distribution of enriched elements within the clusters (Hellman et al. 2000); the greatest anomaly is in the center of each cluster (Fig. 13b). We define the boundaries of clusters by the 0.5 at% Y contour for ARG2.5.

The clusters contain up to 4 at% Y and 1 at% Pb. This enrichment is mainly compensated by a decrease in Zr (Fig. 13b). The three-dimensional distribution of ^{207}Pb and ^{206}Pb is projected in Figure 15b and includes a large contribution from background. For each individual atom, it is not possible to distinguish peak from background and thus the ATP images cannot be background corrected. However, peak counts from spectra are corrected for background. It is significant that after background correction, all detectable Pb is concentrated in the clusters and no Pb is detected outside the clusters (Fig. 6). Thus the Pb atoms shown Figure 15b that are outside of the cluster boundaries (Fig. 15c) are actually background counts. Yttrium is also concentrated in the clusters and it is possible that most of the Y atoms outside of clusters are also background. In contrast, no zoning is seen in U or Th. Thus, the Pb is unsupported, meaning that the present locations of daughter atoms of Pb do not correlate at nanometer-scale to the locations of parent atoms of U and Th. In contrast, the SIMS data indicate that Pb is supported at micrometer-scale; Pb is radiogenic and consistent with the concentrations of U and Th. This apparent contradiction also exists for the clusters in JH4.4 and will be discussed further after presentation of the Pb isotope ratios from APT and discussion of the effects of radiation damage.

Lead concentrations are higher in the clusters of ARG2.5 (~1 at%) than in JH4.4 (0.08 at%) and the signal/background ratio is 2.0 for ^{207}Pb inside clusters, the highest seen in this study.

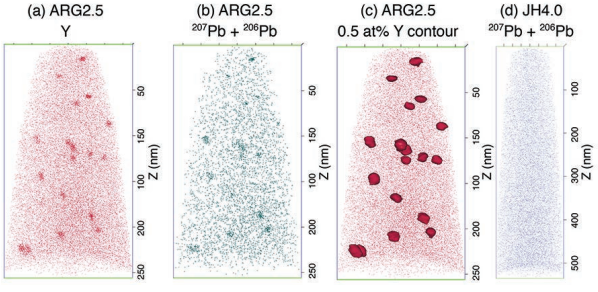

FIGURE 15. Atom probe tomography (APT) showing the distribution of Y and Pb atoms. (**a**) Single atoms and clusters of Y within a 250 nm long needle-shaped specimen of ARG2.5. (**b**) Single atoms and clusters of Pb. (**c**) Domains with >0.5 at% Y. Figure 6 shows that there are no detectable Pb atoms outside of clusters in ARG2.5 and that those spots are background counts; background correction is not possible in APT images. (**d**) Projection of atoms for Pb in the 500 nm long specimen of JH4.0 shown in Figure 5b. Parts **a**–**c** can be viewed as rotating three-dimension movies in the online Supplemental Material[1].

These clusters are not homogeneously distributed throughout the volume investigated. One specimen with 1×10^7 ions detected contains 13 clusters and another with 0.9×10^7 ions contains only one. The ions-counted/cluster ratios vary by more than a factor of 10 (7.7×10^5 to 9×10^6). Not surprisingly, the smallest specimens have the extreme ratios; data for larger specimens average the grouped domains of variable cluster density. Despite a smaller cumulative data set for ARG2.5 (7×10^7 ions), the ^{207}Pb/^{206}Pb ratio can be estimated with comparable precision in this zircon because of higher signal/noise. Among the total ions counted in the Pb-rich clusters of the three specimens with more than one cluster from ARG2.5, there were 1135 atoms of ^{206}Pb and 191 atoms of ^{207}Pb detected for a ^{207}Pb/^{206}Pb ratio of 0.17 ± 0.03 (2 SD). Because all of the Pb detected in these specimens is concentrated in the clusters and no Pb is found outside the 0.5 at% Y contour, this ratio represents the full volume of the specimens.

DISCUSSION

Radiation damage in zircon

The clusters in JH4.4 and ARG2.5 are proposed to result from diffusion of incompatible and less compatible elements into ~10 nm-scale amorphous domains created by α-recoil during U-series and Th-series radioactive decay (Valley et al. 2012, 2014a). This α-decay hypothesis has several testable consequences. During radioactive decay, each atom of ^{238}U, ^{235}U, or ^{232}Th begins a complex decay chain that includes eight, seven, or six α-decay events (and up to six β-decay events) culminating in daughter atoms of ^{206}Pb, ^{207}Pb, or ^{208}Pb, respectively. For each α-decay, an α-particle is emitted that travels distances of 10 000 to 20 000 nm, dissipates its energy through elastic collisions and causes a small number of atomic displacements (damage). The more-massive, but lower energy, daughter atom recoils 20–40 nm and creates approximately 10 times more damage and increase of the zircon unit-cell volume forming a small low-density amorphous domain surrounded by a halo of interstitials (Ewing et al. 2000, 2003; Smye et al. 2014). Thus, the decay of one atom of ^{238}U to ^{206}Pb proceeds through eight α-decay events (and six β-decay events) and a majority of the radiation damage is concentrated in eight α-recoil domains that form sequentially, separated by distances of 20–40 nm/each.

The spatial distribution of vacancies formed in a single α-recoil cascade can be calculated based on the binary collision approximation (Ewing et al. 2003) or using molecular dynamics simulations (Trachenko et al. 2002; Devanathan et al. 2006). The result is a complex branching series of knock-on collisions with >1000 atomic displacements. For purposes of estimating bulk-mineral properties and percolation, the damaged domain of a single α-recoil has been variously modeled as a sphere as small as 3 nm in diameter (Trachenko et al. 2003, 2004; Palenik et al. 2003) or a cylinder up to 2.5 nm diameter × 40 nm long (Jonckheere and Gögen 2001; Ketcham et al. 2013), but the boundaries are indistinct and damage can extend further. Domains of α-recoil damage and single fission tracks have been imaged by TEM (Miller and Ewing 1993; Ewing et al. 2003; Utsunomiya et al. 2004; Li et al. 2014). However, the shape of the path of highest defect density and processes of defect recombination are not well understood. The size and shape of amorphous domains caused

by a single recoil in natural zircons will be significantly modified by short- and long-term processes. The shapes of clusters determined by APT may be strongly influenced by annealing and thus better represent actual mineral properties that affect geochemical retentiveness during the life of a zircon crystal than theoretical models of α-recoil.

The dose of α-decay events experienced per unit weight of zircon can be calculated from the concentrations of U and Th, and the age (Palenik et al. 2003). The calculated dose represents the total radiation emitted during the life of the zircon and would only represent the actually accumulated amount of damage in a zircon in the absence of healing. Fortunately for geochemists, zircons continuously self-heal at relatively low temperatures. Damage from α-recoil heals by both rapid and long-term processes including defect recovery, epitaxial growth, and recrystallization (Ewing et al. 2003). Damage is thought to anneal above 200–300 °C on geologic timescales, although annealing also depends on water fugacity and the initial damaged state; heavily damaged domains may be slower to anneal (Davis and Krogh 2000; Nasdala et al. 2001b; Ewing et al. 2003; Geisler et al. 2007). Thus, in addition to calculating the total dose, it is desirable to estimate the amount of actual damage in a domain of interest. For zircons below the first percolation point, the amount of preserved radiation damage has been estimated from broadening and shifting toward lower wavenumber of Raman bands as measured in reflectance mode at 1 μm-scale (Zhang et al. 2000; Nasdala et al. 2001b, 2003; Pidgeon et al. 2013; Gao et al. 2014; Wang et al. 2014).

The calculated α-doses for zircons of this study are 4.44×10^{15}, 3.84×10^{15}, and 8.05×10^{15} α-events/mg for the domains nearest to the APT-specimen lift-outs in JH4.4, JH4.0, and ARG2.5, respectively. The older zircons experienced less α-decay due to lower [U] and [Th]. In general, low [U] and [Th] values below a few hundreds of part per millions are characteristic of zircons yielding concordant Archean or Hadean ages for this reason. The doses for the three sample zircons are all above the first percolation point, and amorphous domains would form continuous pathways if all damage was retained. However, their thermal history shows that at least some damage has annealed.

All of the Jack Hills detrital zircons have experienced the same temperatures since sedimentary deposition (ca. 3 Ga), including metamorphism at ~500 °C at ca. 2.6 Ga, which would have annealed earlier radiation damage. Pidgeon (2014) assigns a radiation-damage age of 1120 ± 130 Ma to all Jack Hills detrital zircons suggesting that they were fully annealed at 1120 Ma and have accrued damage since that time. If correct, then the analyzed domains of both JH4.4 and JH4.0 have actual damage equivalent to 6.6×10^{14} α-decays/mg at present, well below the first percolation point (2×10^{15} α-decays/mg). The SIMS data show that JH4.4 and JH4.0 are concordant and have not lost Pb at micrometer-scale, which is consistent with thermal histories that prevented accumulation of high levels of radiation damage at any time. In contrast, more radiation damage is reported in zircons from 3.3 and 2.6 Ga granitoids adjacent to the Jack Hills metasedimentary belt (Pidgeon and Wilde 1998; Nasdala et al. 2001b; Utsunomiya et al. 2007). These zircons share the post-2.6 Ga thermal history of detrital Jack Hills zircons, but they contain higher concentrations of U and Th, and experienced higher radiation doses. The higher levels of radiation damage in the zircons studied from granitoids may reflect sorting during sample selection or preferential destruction of metamict zircons during sedimentary transport, which would systematically remove damaged zircons from the detrital suite that was analyzed. As will be discussed below, the low levels of radiation damage and the absence of Pb-mobility at the micrometer-scale, demonstrated here for detrital zircons, indicate that compositions measured by SIMS, including U-Pb age, trace elements and $\delta^{18}O$, are primary and magmatic in origin.

Genesis of clusters

The clusters found in two of the four igneous zircons that have been analyzed to date by APT (this study; Blum et al. 2014) are attributed to reheating and diffusion into amorphous domains caused by α-recoil (Valley et al. 2012, 2014a). This model has only been briefly outlined in previous publications and raises several questions.

Could the clusters in igneous zircons be primary growth features? Zircons sometimes contain common Pb, which can be concentrated in crystal defects or inclusions. The valence of Pb is 2+ for the oxygen fugacities typically found in the Earth's crust, and Pb^{2+} is too large (ionic radius 0.129 nm) to substitute for Zr^{4+} (0.084 nm) (Shannon 1976). Possibly, radiogenic Pb^{4+} (0.094 nm) forms during annealing and substitutes into nano-domains within some zircons (Utsunomiya et al. 2004). For the zircons of this study, the possibility that common Pb was trapped in clusters at the time the zircon crystallized is tested by the $^{207}Pb/^{206}Pb$ ratios. In each of the three zircons, the $^{207}Pb/^{206}Pb$ ratios for the full volume of the APT specimens (within and outside of clusters) are within analytical error of the value for the much larger volume measured by SIMS (Table 3). The agreement of $^{207}Pb/^{206}Pb$ ratios measured by the two techniques and the low common Pb ($^{204}Pb/^{206}Pb < 1 \times 10^{-4}$) measured by SIMS prove that the Pb formed by radioactive decay inside the zircon over an extended period of time. The $^{207}Pb/^{206}Pb$ ratio of 0.17 required 2.5 b.y. to form in ARG2.5. As discussed below, the surprisingly high-$^{207}Pb/^{206}Pb$ ratio of 1.2 in clusters from JH4.4 supports the model that radiogenic Pb was concentrated in clusters at 3.4 Ga following 1 b.y. of radioactive decay. In both of these zircons the $^{207}Pb/^{206}Pb$ ratios rule out the possibility that the clusters formed at the same time as the host zircons. For the volumes inside of clusters, Pb is concentrated, but there is no comparable concentration of U and Th. Thus, the Pb is both radiogenic and unsupported by parent isotopes. A process of selective concentration is required that operated after enough time passed for radioactive decay to form the Pb.

Could the clusters have exsolved from an originally homogeneous igneous zircon after ingrowth of radiogenic Pb? For JH4.4, 12 elements analyzed by APT are shown to be concentrated in the clusters. In addition to Y, eight heavy rare earth elements (HREEs), Pb, Al, and Ca are present at higher levels in the clusters than in surrounding zircon (Table 1; Fig. 13a). The concentrations of Zr and Hf are lower to compensate. There may also be a small change in [Si]. A normalized plot of the eight HREEs parallels the SIMS data for these zircons (Fig. 11a) with an average enrichment factor of 58. The light REEs (LREEs), which have lower concentrations by SIMS (<18 ppmw), were not detected within the clusters by APT. The REEs and Y are less compatible in zircon

at lower temperatures. Pb, Ca, and Al are incompatible in zircon and often correlated to radiation damage and alteration (Rayner et al. 2005; Geisler et al. 2007). Thus these elements show a preference to partition into defects or amorphous domains more than crystalline zircon. The formula of the clusters in JH4.4 would be $(Zr_{0.78}YREE_{0.38}P_{0.01}Si_{0.91})_{2.08}O_4$ if APT data were normalized to four O atoms. This cation-excess formula does not fit known zircon solid solutions or any other mineral. For instance, xenotime substitution requires that the number of P atoms is equivalent to the number of trivalent (Y + REE) atoms. The APT data also rule out the presence of nano-crystals of ZrO_2 and SiO_2 that might form due to radiation damage. Thus, the clusters are best explained as originally forming non-stoichiometric amorphous zones within zircon that have become enriched in less compatible elements (but not U and P) at some time after formation of the zircon.

Do the clusters retain their original size, shape, and orientation? A comparison of the volumes of individual clusters in ARG2.5 and JH4.4 has been made using a 0.5 at% Y contour for both zircons. This value is the same as for the analyses presented above for ARG2.5, but for the sake of comparison, it is less than the 3 at% Y value used for determining the composition of JH4.4. Figure 16 shows the comparison of cluster volumes. The distributions are quite different with the JH4.4 showing a bimodal distribution (~100–400 and 900–2000 nm^3/cluster) and the ARG2.5 showing volumes of ~300–600 nm^3. The average volumes in JH4.4 are: 241 nm^3 for 208 clusters smaller than 570 nm^3; 1483 nm^3 for 183 clusters larger than 740 nm^3 (none are between 570 and 740 nm^3); and 823 nm^3 for all 391 clusters. In contrast the 35 clusters in ARG2.5 show a nearly normal distribution averaging 437 nm^3. It is likely that any early-formed amorphous domains in JH4.4 were annealed during prolonged metamorphism at 2.6 Ga, as seen by high-resolution high-angle annular dark-field scanning transmission electron microscopy (HAAD-STEM) in an undated detrital zircon from a nearby outcrop (Utsunomiya et al. 2004). The details of individual clusters and the bimodality of zircons in JH4.4 are the subject of ongoing study. At present, we interpret these differences in size, as well as those in shape and orientation described earlier, as due to modification of clusters after their formation. APT provides new information for assessing the processes of annealing as well as percolation and the fidelity of geochemical data in altered zircons.

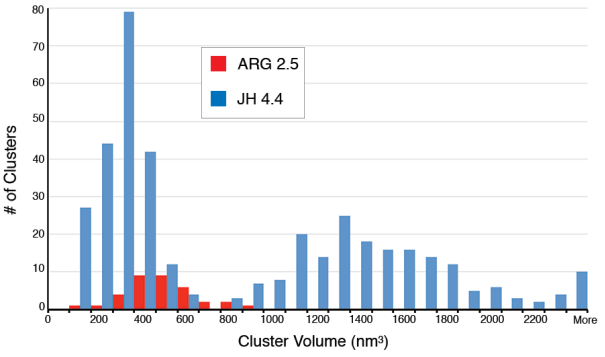

FIGURE 16. Histogram of cluster volumes for JH4.4 and ARG2.5 defined by the 0.5 at% Y contour in each zircon. A total of 391 clusters are detected in JH4.4 by this criteria compared to 35 in ARG2.5 due to the larger specimens that were analyzed by APT. In contrast to ARG2.5, the JH4.4 zircon was metamorphosed and annealed at 3400 vs. 29 Ma, which allowed more time for changes in size, shape, and orientation.

Timing of zircon crystallization and cluster formation

The timing of zircon crystallization and cluster formation can be determined from the $^{207}Pb/^{206}Pb$ ratios. The APT and SIMS data are complementary and together give a more complete history than either data set alone. JH4.0 has no clusters and the $^{207}Pb/^{206}Pb$ ratios are the same by APT (0.42 ± 0.07) and by SIMS (0.4269), consistent with the Pb/Pb age of 4.007 Ga. For ARG2.5, the $^{207}Pb/^{206}Pb$ ratio of the entire specimen by APT is the same as in clusters because no Pb is detected outside of the clusters. This ratio by APT (0.17 ± 0.03) is in excellent agreement with 0.1684 measured by SIMS and yields a Pb/Pb model age of 2.5 Ga. The Pb/Pb model age assumes that Pb mobility from the matrix to clusters was recent, consistent with the 29 Ma age of the host Vipoint pluton and the magmatic zircon rim. In other words, U- and Th-decay proceeded for 2.5 b.y. and then all of the radiogenic Pb migrated to the clusters. If Pb migration had been earlier, then U and Th decay would have produced measurable Pb outside of the clusters.

For JH4.4, the average $^{207}Pb/^{206}Pb$ ratio of the full APT specimens is 0.52 ± 0.04, within uncertainty of 0.5472 measured by SIMS, and consistent with the Pb/Pb model age of 4.374 Ga, and the concordant U-Pb ages by SIMS. Outside of the clusters, but within the core of the zircon, the ratio is 0.3 ± 0.05 by APT, consistent within uncertainty of 0.2867 by SIMS and a model age of 3.4 Ga for the younger rim of the zircon. However, no SIMS data match this ratio (0.3) within the core of the zircon because the relatively large volume analyzed by SIMS homogenizes the compositions of clusters and zircon outside of clusters. Inside of the clusters, the $^{207}Pb/^{206}Pb$ ratio is 1.2, which is much higher than SIMS data for any of the Hadean zircons. This ratio cannot be interpreted with a model age assuming recent Pb loss. A chord from the origin with this slope (dashed in Fig. 9a) would suggest an age of ca. 5.5 Ga, which is older than the Earth; such a model is not correct. The calculation of a standard model age is not appropriate because: (1) the Pb mobility was not recent, and (2) more critically, early-formed radiogenic Pb migrated into clusters. The APT data give only a $^{207}Pb/^{206}Pb$ ratio, which defines the slope in Figure 9a, but not the Y-intercept. If, instead of passing through the origin, a line with this slope is drawn from the crystallization age of 4.4 Ga determined by SIMS, then the lower intercept is at 3.4 Ga (upper dashed line in Fig. 9a), which is the age of the rim-forming event. A model for zircon growth at 4.374 Ga and cluster formation at 3.4 Ga thus fits the data perfectly. The radiogenic Pb that formed between 4.374 and 3.4 Ga is enriched in ^{207}Pb because there was proportionately more of the shorter-lived parent, ^{235}U, on the early Earth. The $^{207}Pb/^{206}Pb$ ratio can be calculated, and for a zircon that crystallized at 4.374 Ga, the ratio will be 1.2 at 3.4 Ga, based on the half-lives of ^{238}U and ^{235}U, and the modern ratio of $^{238}U/^{235}U = 137.82$. The agreement of measured and calculated ratios strongly supports the interpretation that JH4.4 crystallized at 4.374 and that one billion years later, all of the radiogenic Pb migrated to the clus-

ters. Thus, the clusters in JH4.4 contain less Pb than clusters in ARG2.5 because of lower [U] and [Th], and also because they only represent 1 b.y. of radioactive decay vs. 2.5 b.y. From 3.4 Ga until today, radioactive decay has continued in JH4.4, creating a $^{207}Pb/^{206}Pb$ ratio of 0.3 outside of clusters, but the ratio has not been significantly changed inside the clusters due to the ~40 times higher ratio of [Pb]/([U] + [Th]).

The α-recoil model

The α-recoil model for genesis of clusters in zircon (Valley et al. 2012, 2014a) proposes late migration of incompatible elements into amorphous domains caused by α-recoil at the time of high-grade reheating events. This model suggests several tests that could either strengthen or refute it. As discussed above, the decay chains for individual parent atoms of ^{238}U, ^{235}U, or ^{232}Th will create groups of 8, 7, or 6 spatially related domains of α-recoil damage, respectively. Furthermore, these domains will form sequentially with predictable average distances based on mineralogy, the energy of the daughter atom and possibly the crystallographic orientation of the recoil. Visual inspection of the rotating APT movies for clusters in JH4.4 and ARG2.5 shows clear variability in the spacing of clusters and is permissive of groups of 6 to 8, although many domains extend beyond the analyzed boundaries of the specimens and many groups are smaller than 6. The abundances of the three parent isotopes at the time of cluster formation further predict the proportions of different group size and groups of eight clusters should be most common. The abundance and inter-cluster distances are consistent with this model, but the data set is not presently large enough to test this hypothesis.

The high [Pb] within clusters is not predicted if all domains of α-recoil damage are equally preserved. Only one atom of radiogenic Pb is produced for every 6–8 α-recoil events, yet the clusters in JH4.4 contain on average ~150 atoms of Pb/cluster and in ARG2.5, there are ~100 atoms of Pb/cluster. If the clusters occupy domains of α-recoil, then <0.1% of the α-recoil events has formed a cluster. This is readily explained if the zircons were continuously annealed during their early history (consistent with concordant ages) and only a small percentage of newly formed, damaged domains were amorphous at the time of reheating and mobilization of Pb.

If these zircons were continuously annealed, then the radiation damage never reached the first percolation point and volume diffusion through crystalline zircon is required to explain Pb and YREE migration into clusters. For the inter-cluster spacing of JH4.4 and ARG2.5, diffusion distances on the scale of 20 nm would be sufficient to concentrate less compatible elements in the amorphous domains created by α-recoil. Rates of Yb (and other REE) diffusion are predicted by experimental data (Cherniak 2010) and are too slow below 500 °C to accomplish this concentration. However, heating to 800 °C for ~2 m.y. would be sufficient for REEs to diffuse 20 nm. Pb diffusion is faster and any reheating that concentrated REEs could efficiently scavenge Pb. Compatible elements, including U and Th, have no energetic drive to migrate by diffusion. There is no younger rim on JH4.0 and the lack of reheating explains the absence of clusters in this zircon. The igneous rims on grains JH4.4 (3.4 Ga) and ARG2.5 (29 Ma) document periods when these zircons were reheated as xenocrysts in younger magmas. Such magmatic recycling generally proceeds during high-grade metamorphism in the deep crust. This high-temperature event is documented at 29 Ma when the rim of ARG2.5 formed in the crystallizing Vipoint pluton (Strickland et al. 2011a, 2011b). Thus a Pb/Pb model age assuming recent Pb loss explains the $^{207}Pb/^{206}Pb$ ratio inside clusters. This model predicts that only ~2 ppm of radiogenic Pb has formed over the past 29 m.y. in the regions outside of clusters, and this concentration is too small to be detected by APT. If the age of reheating was significantly older than 100 Ma, there should be Pb detected outside of the clusters by APT.

The SIMS age for the rim on JH4.4 documents reheating at ca. 3.4 Ga. In contrast to ARG2.5, JH4.4 is detrital, and the parent rock and field relations are unknown. The 3.4 Ga rim could be related to the intrusion of Dugel orthogneisses (3.38–3.35 Ga; Kinny and Nutman 1996; Pidgeon and Wilde 1998; Cavosie et al. 2004) that outcrop adjacent to the Jack Hills or to igneous events elsewhere. The age of 3.4 Ga is indicated in two ways by the APT $^{207}Pb/^{206}Pb$ ratios. The ratio of 0.3 outside of the clusters required 3.4 b.y. to accumulate. Likewise the unusually high ratio of 1.2 from inside of the clusters indicates a shorter period of radioactive decay early in Earth history, which, if it started at 4.374 Ga terminated 1 b.y. later at 3.4 Ga. Thus for both ARG2.5 and JH4.4, the age of the reheating event could be deduced from the APT results even if the younger rim was abraded away during sedimentary transport. More generally, APT data offer a new approach for identifying and constraining otherwise cryptic thermal events due to magmatism or high-grade metamorphism.

One final test of the α-recoil model relates to the annealing rate of radiation damage. Healing of radiation damage occurs by multiple complex processes that vary with the extent of damage and are faster under hydrous conditions (Pidgeon et al. 1966). Beam broadening and peak shifts by Raman-spectroscopy show that both naturally and experimentally damaged zircons experience hysteresis in annealing. In addition, amorphous $ZrSiO_4$, oxides, micro-strain, voids, dislocation loops, and point defects can form (Ewing et al. 2003; Nasdala et al. 2003). It is generally agreed that long-term annealing of α-recoil damage begins at low temperature and is nearly complete for steady-state conditions above ~300 °C, and yet calculations of volume diffusion distances (~20 nm) for REEs into the clusters suggest temperatures of ~800 °C.

How can damaged domains survive at 800 °C to concentrate incompatible elements? The results discussed above indicate that the majority of recoil-damaged domains that formed in JH4.4 and ARG2.5 are not represented by clusters and thus were probably annealed before the reheating event. This suggests that temperatures were kept above 200–300 °C and annealing was at steady state. In this scenario, new amorphous domains formed and were annealed continuously, perhaps at timescales of 10–100 m.y. Thus there was always a small population of newly formed unannealed domains and they persisted long enough to concentrate less compatible elements when reheating opened the zircon to short-distance diffusion. This prediction is that the time required to anneal α-recoil damaged domains is longer than ~2 m.y., which is necessary for Pb and Y-REEs to diffuse 20 nm in zircon. The process of radiation damage and annealing is not a reversible reaction and does not follow the same rate law as

volume diffusion. Slow annealing at m.y.-timescales, even at high temperature, is consistent with estimates for the half-life of a α-recoil cascade (Lumpkin and Ewing 1988; Ewing et al. 2003). Thus, the zircons of this study maintained a steady-state density of α-recoil damage below the first percolation over hundreds to thousands of m.y. and the relatively short reheating events were not sufficient to remove all of the domains of α-recoil damage.

Fidelity of the zircon record

Cavosie et al. (2006) defined type-1 and type-2 domains within zircon based on chondrite-normalized values of LREE measured by SIMS. Type-2 zircons (La > 1 and Pr > 10) are interpreted as disturbed with REE mobility probably enhanced by radiation damage. The zircons of this study are type-1 by this definition and do not show evidence for trace element mobility at the 10 μm-scale of a SIMS analysis pit. The demonstration by APT that these ancient zircons were closed systems to mobility of Pb, Y, and REEs at the scale of SIMS analyses (10–25 μm spots) supports the conclusion that type-1 zircons preserve magmatic compositions and it removes one of the long-lasting challenges to the accuracy of in situ U-Pb geochronology. These results provide enhanced confidence in criteria based on correlating CL patterns and U/Pb age concordance to identify unaltered domains within zircon.

Oxygen isotopes

Oxygen isotope ratios in zircons, measured in situ by SIMS, can identify the parent rock and its protolith as well as the later thermal and alteration history (Valley 2003). All $\delta^{18}O$(Zrn) values in the three grains studied are within uncertainty of mantle-like values, 4.7 to 5.9‰ (Table 4). Likewise, 4.35 to 3.9 Ga zircons from the Moon average $\delta^{18}O = 5.61 \pm 0.07$‰ (Valley et al. 2014b). Crystalline zircon is highly retentive of primary $\delta^{18}O$ values, but above the first percolation point, zircons have a large percentage of amorphous domains and frequently become altered (Valley et al. 1994, 2005).

In contrast to the primitive magmatic $\delta^{18}O$ values in zoned-zircon domains of this study, three analyses of the distinctive (dark CL) disturbed domains within JH4.0 and JH4.4 are lower in $\delta^{18}O$ (4.1 to 3.5‰). Disturbed areas within zircon crystals frequently have such distinctive CL patterns and can result

Table 4. Oxygen isotope analyses by SIMS of zircons JH4.4, JH4.0, and ARG2.5, and quartz inclusions in JH4.4

Sample analysis spot	Age Ma[a]	Loc.[b]	$\delta^{18}O$ VSMOW[c]	2 SD[d]	$\delta^{17}O$ VSMOW[c]	2 SD[d]	$\Delta^{17}O$	2 SD[d]	Ref.[e]
			ARG2.5 (ARG05-28-2)						
ARG05-28-2	2542	core							1,2
	–	mantle	6.21	0.23					2
	–	mantle	5.38	0.23					2
			JH4.0 [01JH13b-8.4 (2.5M)]						
July 19, 2006									
2.5M 8.4.1	4007	mantle	5.81	0.23					3
2.5M 8.4.2	–	dist. core	4.09	0.23					3
2.5M 8.4.3	4007	mantle	5.95	0.23					3
2.5M 8.4.4	4007	mantle	5.84	0.23					3
	avg. Zrn rim (n=3)		5.87	0.15					
Dec. 21, 2006									
01JH13b_2.5M	8-4	mantle	6.01	0.15	3.04	0.28	–0.09	0.26	4
			JH4.4 [01JH-36-69 (5M)]						
July 28, 2006									
5M 69.1	4374	core	4.73	0.34					5
5M 69.2	4374	core	4.47	0.34					5
5M 69.3	4374	core	4.94	0.34					5
5M 69.4	4374	core	4.78	0.34					5
5M 69.5	~3400	rim	5.73	0.34					5
5M 69.6	~3400	rim	5.36	0.34					5
5M 69.7	~3400	rim	5.87	0.34					5
5M 69.8	~3400	rim	5.47	0.34					5
5M 69.9	–	dist.	3.54	0.34					5
5M 69.10	4374	core	5.00	0.34					5
5M 69.11	4374	core	4.81	0.34					5
5M 69.Q1	–	Qz incl.	12.49	0.28					6
5M 69.Q2	–	Qz incl.	12.43	0.28					6
5M 69.Q3	–	Qz incl.	12.84	0.28					6
	avg. Zrn core (n=6)		4.79	0.37					
	avg. Zrn rim (n=4)		5.60	0.47					
	avg. Qz (n=3)		12.59	0.44					
Dec. 21, 2006									
01JH36 69-1	4374	core	4.88	0.25	2.59	0.13	0.05	0.21	4,5
01JH36 69-2	4374	core	4.84	0.25	2.56	0.13	0.05	0.21	4,5
01JH36 69-3	4374	core	4.66	0.25	2.53	0.13	0.10	0.21	4,5
01JH36 69-4	–	dist.	3.56	0.25	2.03	0.13	0.18	0.21	4,5

[a] $^{207}Pb/^{206}Pb$ age. Ma = Mega annum.
[b] Loc. = location within zircon: core, rim, mantle, incl. = mineral inclusion, dist. = disturbed zircon domain.
[c] Corrected value, VSMOW.
[d] The 2 SD of an individual analysis is based on the spot-to-spot reproducibility of two "bracketing sets" of standard analyses (8 spots). A "bracketing set" consists of four analyses of KIM-5 (UWQ-1 for Qz), before and after every 10–12 sample analyses. The 2 SD listed with the sample averages is based on measured δ if at least three measurements were made.
[e] References: (1) Strickland, pers. comm. 2011; (2) Strickland et al. 2011b; (3) Cavosie et al. 2005; Ushikubo et al. 2008; (4) Valley et al. 2007; (5) Valley et al. 2014a; (6) this study.

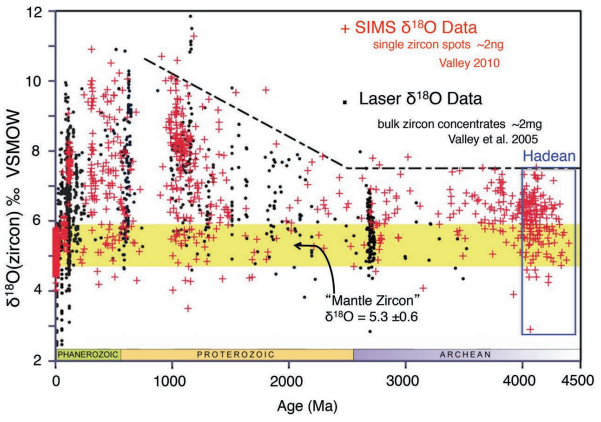

FIGURE 17. Values of $\delta^{18}O$ for magmatic of zircons with low-radiation damage vs. U-Pb age. Laser data were analyzed for $\delta^{18}O$ by bulk fluorination of ~2 mg samples (typically a few hundred zircon grains) and there is one spot per rock. Radiation damage was evaluated by either magnetic separation of low-mag. zircons or soaking overnight in HF (Valley et al. 2005). SIMS $\delta^{18}O$ data were analyzed in situ and may include tens of analyses from a single rock (Valley 2010). SIMS $\delta^{18}O$ analyses are from volumes ~10^6 times smaller than by laser and are typically less precise (±0.3 to 0.6‰ vs. ±0.1‰, 2 SD). Zircons in primitive magmas and in high-temperature equilibrium with mantle values of $\delta^{18}O$ fall in the range of 4.7 to 5.9‰ (5.3 ± 0.6‰). Values above this range result from protoliths that underwent low temperature aqueous exchange at the surface of the Earth. Values above 7.5‰ are rare in the Archean for pristine magmatic zircons, but common for metamorphic and altered zircon. Values below 4.7‰ largely result if protoliths were hydrothermally altered. Hadean and Archean $\delta^{18}O$(zircon) values above 6‰ indicate that the surface of the Earth was cool and hospitable to life as early as 4.3 Ga.

from accumulated radiation damage that shortcuts diffusion and opens the crystal structure to exchange and alteration of primary $\delta^{18}O$ values (Valley et al. 2005; Cavosie et al. 2005). Alternatively, Pidgeon (1992) reports a similar CL texture for "unzoned" domains within zircons from a late granite cutting Jack Hills metasediments (W-34) and, based on measured dates in these domains, attributes them to subsolidus recrystallization synchronous to intrusion and metamorphism at ca. 2.6 Ga when the zircon was too young to have accrued significant radiation damage. However, radiation damage by itself does not alter U-Pb dates; some additional alteration process is required for Pb mobility. It is possible that disturbed zircon domains in W-34 formed later than their U-Pb date would suggest. In JH4.4, the reduced crystallinity (measured by EBSD) of disturbed domains supports the radiation damage hypothesis (Valley et al. 2014a), but either way, disturbed domains cannot be assumed to preserve primary igneous compositions. Furthermore, accurate analysis by SIMS is not possible for metamict zircon without equivalent radiation-damaged standards that do not presently exist. In this study, the three $\delta^{18}O$ values for disturbed domains in JH4.4 will not be considered further.

Oxygen three isotopes ($\delta^{18}O$ and $\delta^{17}O$) have been measured in JH4.4 and JH4.0 and other Hadean zircons from the Jack Hills (Fig. 10) (Valley et al. 2007, 2014a). Values of $\Delta^{17}O$ are normalized relative to bulk silicate Earth (defined as $\Delta^{17}O$ = 0‰ for the KIM-5 zircon standard, a mantle megacryst) and are precise to ±0.22 (2 SD, N = 28, 2SE = 0.04‰). Thirty-six Jack Hills zircons with ages from 4.0 to 4.35 Ga average $\Delta^{17}O$ = –0.05 ± 0.24‰ (2 SD, N = 44). The combination of $\Delta^{17}O$ = 0, positive Ce anomaly, and low [Ti] provides a signature for terrestrial zircons (Valley et al. 2014b), ruling out an extra-terrestrial origin for the Jack Hills detrital zircons, including JH4.4 and JH4.0. These $\Delta^{17}O$ values reflect early homogenization of the Earth following accretion, presumably by wholesale melting related to formation of the Moon and the Earth's core (Rumble et al. 2013; Valley et al. 2014a).

Primitive $\delta^{18}O$ values are common in the detrital Hadean suite, but many of the zircons are mildly elevated up to 7.5‰ (Fig. 17) (Peck et al. 2001; Valley et al. 2005; Cavosie et al. 2005, 2007; Trail et al. 2007; Harrison et al. 2008; Harrison 2009). These mildly elevated values of $\delta^{18}O$ provide strong support for the Cool Early Earth hypothesis, which proposes that protoliths of zircon-forming magmas underwent aqueous alteration at low temperatures and that habitable liquid-water oceans condensed on Earth before 4.3 Ga (Valley et al. 2002).

IMPLICATIONS

The complementary data from secondary ion mass spectrometry (SIMS) and atom probe tomography (APT) document atom-scale isotope and trace element distribution leading to enhanced thermochronology of Hadean and Archean zircons. APT shows that Pb, Y, and REEs are concentrated in ~10 nm clusters in two xenocryst zircons (4.4 and 2.5 Ga), which have younger rims that document magmatic reheating. Quantitative measurements of the $^{207}Pb/^{206}Pb$ ratios provide nano-geochronological information. Lead in the clusters is radiogenic and unsupported by parent isotopes as predicted by the α-recoil model for their genesis. This model proposes that incompatible elements diffused during reheating into amorphous domains damaged by α-recoil (Valley et al. 2014a). In addition to JH4.0 of this study, a fourth zircon (14Q4 from the Moon, 4.35 Ga) has been studied by APT (Blum et al. 2014), and neither of these zircons have younger rims or contain clusters ruling out later magmatic reheating or high-grade metamorphism.

This first combined nano- and micro-geochronology study of multiple zircons provides enhanced confidence in criteria for evaluating the fidelity of their geochemical records. Demonstration that Pb mobility occurred at sub-50 nm-scale to form clusters shows that longer-distance Pb transport did not occur and that the much-larger 20 μm-scale volumes analyzed by SIMS were closed systems. The existence of 4.4 Ga zircons, the oldest known from Earth, is confirmed. Likewise, REE spectra and stable isotope ratios are supported as primary, reflecting magmatic compositions. Taken together, these data support models of a more-clement Early Earth than the name Hadean suggests. Differentiated crust existed by 4.4 Ga, just 100 m.y. after the formation of the Moon and Earth's core. The steam atmosphere cooled and precipitated as oceans before 4.3 Ga creating conditions habitable to life as much as 800 m.y. earlier than the oldest known microfossils (Cavosie et al. 2005).

More generally, these new tools are suited for many minerals

of all ages. The ability to analyze insulating as well as electrically conductive materials by APT bridges the gap in capabilities between TEM and SIMS. Single atoms in nano-domains, previously only imaged by TEM, can now be identified by mass and position. Conversely, zoning can be investigated in larger micrometer-scale domains by SIMS, providing context for smaller-scale spatial information. These analytical advances open many new research opportunities of interest to mineralogists and geochemists.

Acknowledgments

The authors thank Brian Hess for sample preparation and polishing; John Fournelle and Phil Gopon for assistance with EPMA and SEM; Noriko Kita and Jim Kern for assistance with SIMS; and David Valley for assistance in fieldwork. John Craven assisted with SIMS analysis in Edinburgh and has been of invaluable assistance in many of the first author's in situ studies of oxygen isotope ratio. We thank Tyler Blum, Kouki Kitajima, Dunyi Liu, Des Moser, Mike Spicuzza, Simon Wilde, and our colleagues at CAMECA in Madison, Wisconsin, for their contributions to these efforts. D.A.R., D.F.L., D.J.L., and T.F.K. are employees of CAMECA who manufactures the LEAP instrument that was used in this study. This research was supported by the U.S. National Science Foundation (EAR-0838058); the U.S. Department of Energy Office of Science, Office of Basic Energy Sciences under Award Number DE-FG02-93ER14389; and the NASA Astrobiology Institute. WiscSIMS is partly supported by NSF-EAR-1053466 and NSF-EAR-1355590.

References cited

Aines, R.D., and Rossman, G.R. (1986) Relationships between radiation damage and trace water in zircon, quartz, and topaz. American Mineralogist, 71, 1186–1193.

Ashwal, L.D., Tucker, R.D., and Zinner, E.K. (1999) Slow cooling of deep crustal granulites and Pb-loss in zircon. Geochimica et Cosmochimica Acta, 63, 2839–2851.

Blavette, D., Grancher, G., and Bostel, A. (1988) Statistical analysis of atom-probe data (I): Derivation of some fine-scale features from frequency distributions for finely dispersed systems. Le Journal de Physique Colloques, 49, C6-433–C6-438.

Blum, T.B., Reinhard, D., Spicuzza, M., Olson, D., Coble, M.A., Cavosie, A., Ushikubo, T., Larson, D., Kelly, T., and Valley, J.W. (2014) Nanoscale isotope mapping of terrestrial and lunar zircons by atom probe tomography. Transactions American Geophysical Union, Fall Meeting, Abstract V34A-06.

Booth, A.L., Kolodny, Y., Chamberlain, C.P., McWilliams, M., Schmitt, A.K., and Wooden, J. (2005) Oxygen isotopic composition and U-Pb discordance in zircon. Geochimica et Cosmochimica Acta, 69, 4895–4905.

Bouvier, A.-S., Ushikubo, T., Kita, N.T., Cavosie, A.J., Kozdon, R., and Valley, J.W. (2012) Li isotopes and trace elements as a petrogenetic tracer in zircon: insights from Archean TTG's and sanukitoids. Contributions to Mineralogy and Petrology, 163, 745–768.

Bunton, J.H., Olson, J.D., Lenz, D., and Kelly, T.F. (2007) Advances in pulsed-laser atom probe: Instrument and specimen design for optimum performance. Microscopy and Microanalysis, 13, 418–427.

Cavosie, A.J. (2005) Geochemistry of >3900 Ma detrital zircons from Jack Hills, Western Australia. Ph.D. thesis, University of Wisconsin-Madison, 387 p.

Cavosie, A.J., Wilde, S.A., Liu, D., Valley, J.W., and Weiblen, P.W. (2004) Internal zoning and U-Th-Pb chemistry of the Jack Hills detrital zircons: A mineral record of early Archean to Mesoproterozoic (4348–1576 Ma) magmatism. Precambrian Research, 135, 251–279.

Cavosie, A.J., Valley, J.W., and Wilde, S.A. (2005) Magmatic $\delta^{18}O$ in 4400-3900 Ma detrital zircons: A record of the alteration and recycling of crust in the Early Archean. Earth and Planetary Science Letters, 235, 663–681.

Cavosie, A.J., Valley, J.W., Wilde, S.A., and E.I.M.F. (2006) Correlated microanalysis of zircon: Trace element, $\delta^{18}O$, and U-Th-Pb isotopic constraints on the igneous origin of complex >3900 Ma detrital grains. Geochimica et Cosmochimica Acta, 70, 5601–5616.

Cavosie, A.J., Valley, J.W., and Wilde, S.A. (2007) The oldest terrestrial mineral record: A review of 4400 to 4000 Ma detrital zircons from the Jack Hills, Western Australia. In M.J. van Kranendonk, R.H. Smithies, and V.C. Bennett, Eds., Earth's Oldest Rocks. Developments in Precambrian Geology, 15, 91–111.

Cerezo, A., and Davin, L. (2007) Aspects of the observation of clusters in the 3-dimensional atom probe. Surface and Interface Analysis, 39, 184–188.

Chakoumakos, B.C., Murakami, T., Lumpkin, G.R., and Ewing, R.C. (1987) Alpha-decay—Induced fracturing in zircon: The transition from the crystalline to the metamict state. Science, 236, 1556–1559.

Cherniak, D.J. (2010) Diffusion in accessory minerals: Zircon, titanite, apatite, monazite and xenotime. Reviews in Mineralogy and Geochemistry, 72, 827–869.

Compston, W.T., and Pidgeon, R.T. (1986) Jack Hills, evidence of more very old detrital zircons in Western Australia. Nature, 321, 766–769.

Condon, D.J., and Schmitz, M.D., Eds. (2013) One hundred years of geochronology. Elements, 9, 3–80.

Corfu, F., Hanchar, J.M., Hoskin, P.W., and Kinny, P. (2003) Atlas of zircon textures. Reviews in Mineralogy and Geochemistry, 53, 469–500.

Currie, L.A. (1968) Limits for qualitative detection and quantitative determination: application to radiochemistry. Analytical Chemistry, 40, 586–592.

Davis, D.W., and Krogh, T.E. (2000) Preferential dissolution of ^{234}U and radiogenic Pb from a-recoil-damaged lattice sites in zircon: Implications for thermal histories and Pb isotopic fractionation in the near surface environment. Chemical Geology, 172, 41–58.

De Geuser, F., Lefebvre, W., and Blavette, D. (2006) 3D atom probe study of solute atoms clustering during natural ageing and pre-ageing of an Al-Mg-Si alloy. Philosophical Magazine Letters, 86, 227–234.

Devanathan, R., Corrales, L.R., Weber, W.J., Chartier, A., and Meis, C. (2006) Molecular dynamics simulation of energetic uranium recoil damage in zircon. Molecular Simulation, 32, 1069–1077.

Ewing, R.C., Meldrum, A., Wang, L., and Wang, S. (2000) Radiation-induced amorphization. Reviews in Mineralogy and Geochemistry, 39, 319–361.

Ewing, R.C., Meldrum, A., Wang, L., Weber, W.J., and Corrales, L.R. (2003) Radiation effects in zircon. Reviews in Mineralogy and Geochemistry, 53, 387–425.

Fu, B., Page, F.Z., Cavosie, A.J., Fournelle, J., Kita, N.T., Lackey, J.S., Wilde, S.A., and Valley, J.W. (2008) Ti-in-zircon thermometry: Applications and limitations. Contributions to Mineralogy and Petrology, 156, 197–215.

Gao, Y.Y., Li, X.H., Griffin, W.L., O'Reilly, S.Y., and Wang, Y.F. (2014) Screening criteria for reliable U–Pb geochronology and oxygen isotope analysis in uranium-rich zircons: A case study from the Suzhou A-type granites, SE China. Lithos, 192, 180–191.

Gault, B., Vurpillot, F., Vella, A., Gilbert, M., Menand, A., and Blavette, D. (2006) Design of a femtosecond laser assisted tomographic atom probe. Review of Scientific Instruments, 77, 043705.

Gault, B., Moody, M.P., De Geuser, F., Haley, D., Stephenson, L.T., and Ringer, S.P. (2009) Origin of the spatial resolution in atom probe microscopy. Applied Physics Letters, 95, 034103/1–8.

Gault, B., Moody, M.P., Cairney, J.M., and Ringer, S.P. (2012) Atom Probe Microscopy. Springer Series in Materials Science, 160, 396 p.

Geisler, T., and Schleicher, H. (2000) Improved U-Th-total Pb dating of zircons by electron microprobe using a simple new background modeling procedure and Ca as a chemical criterion of fluid-induced U-Th-Pb discordance in zircon. Chemical Geology, 163, 269–285.

Geisler, T., Pidgeon, R.T., Kurtz, R., van Bronswijk, W., and Schleicher, H. (2003) Experimental hydrothermal alteration of partially metamict zircon. American Mineralogist, 88, 1496–1513.

Geisler, T., Schaltegger, U., and Tomaschek, F. (2007) Re-equilibration of zircon in aqueous fluids and melts. Elements, 3, 43–50.

Harrison, T.M. (2009) The Hadean crust: evidence from >4 Ga zircons. Annual Review of Earth and Planetary Sciences, 37, 479–505.

Harrison, T.M., Schmitt, A.K., McCulloch, M.T., and Lovera, O.M. (2008) Early (4.5 Ga) formation of terrestrial crust: Lu-Hf, $\delta^{18}O$, and Ti thermometry results for Hadean zircons. Earth and Planetary Science Letters, 268, 476–486.

Heck, P.R., Staderman, F.J., Isheim, D., Auciello, O., Daulton, T.L., Davis, A.M., Elam, J.W., Floss, C., Hiller, J., Larson, D.J., Lewis, J.B., Mane, A., Pellin, M.J., Savina, M.R., Seidman, D.N., and Stephan, T. (2014) Atom-probe analyses of nanodiamonds from Allende. Meteoritics & Planetary Science, 49, 453–467, http://dx.doi.org/10.1111/maps.12265.

Hellman, O.C., Vandenbroucke, J.A., Rusing, J., Isheim, D., and Seidman, D.N. (2000) Analysis of three-dimensional atom-probe data by the proximity histogram. Microscopy and Microanalysis, 6, 437–444.

Hellman, O.C., Rivage, J.B.D., and Seidman, D.N. (2003) Efficient sampling for three-dimensional atom probe microscopy data. Ultramicroscopy, 95, 199–205.

Holden, P., Lanc, P., Ireland, T.R., Harrison, T.M., Foster, J.J., and Bruce, Z. (2009) Mass-spectrometric mining of Hadean zircons by automated SHRIMP multi-collector and single collector U/Pb zircon age dating: The first 100 000 grains. International Journal of Mass Spectrometry, 286, 53–63.

Holland, H.D., and Gottfried, D. (1955) The effect of nuclear radiation on the structure of zircon. Acta Crystallographica, 8, 291–300.

Holmes, A. (1913) The Age of the Earth, 196 p. Harper and Brothers, London.

Hoskin, P.W. (2005) Trace-element composition of hydrothermal zircon and the alteration of Hadean zircon from the Jack Hills, Australia. Geochimica et Cosmochimica Acta, 69, 637–648.

Hoskin, P.W., and Schaltegger, U. (2003) The composition of zircon and igneous and metamorphic petrogenesis. Reviews in Mineralogy and Geochemistry, 53, 27–62.

Hyde, J.M., and English, C.A. (2000) An analysis of the structure of irradiation induced Cu-enriched clusters in low and high nickel welds. Materials Research Society Proceedings, 650, R6-6. Cambridge University Press, U.K.

Hyde, J.M., Marquis, E.A., Wilford, K.B., and Williams, T.J. (2011) A sensitivity analysis of the maximum separation method for the characterisation of solute clusters. Ultramicroscopy, 111, 440–447.

Ireland, T.R., and Williams, I.S. (2003) Considerations in zircon geochronology by SIMS. Reviews in Mineralogy and Geochemistry, 53, 215–241.
Jonckheere, R., and Gögen, K. (2001) A Monte-Carlo calculation of the size distribution of latent alpha-recoil tracks. Nuclear Instruments and Methods in Physics Research Section B: Beam Interactions with Materials and Atoms, 183, 347–357.
Kellogg, G.L., and Tsong, T.T. (1980) Pulsed-laser atom-probe field-ion microscopy. Journal of Applied Physics, 51, 1184–1194.
Kelly, T.F., and Larson D.J. (2012) Atom probe tomography. Annual Review of Materials Research, 42, 1–31.
Kelly, T.F., Voelkl, E., and Geiser, B.P. (2009) Practical determination of spatial resolution in atom probe tomography. Microscopy and Microanalysis, 15, 12–13.
Ketcham, R.A., Guenthner, W.R., and Reiners, P.W. (2013) Geometric analysis of radiation damage connectivity in zircon, and its implications for helium diffusion. American Mineralogist, 98, 350–360.
King, E.M., Valley, J.W., Davis, D.W., and Edwards, G.R. (1998) Oxygen isotope ratios of Archean plutonic zircons from granite–greenstone belts of the Superior Province: indicator of magmatic source. Precambrian Research, 92, 365–387.
Kinny, P.D., and Nutman, A.P. (1996) Zirconology of the Meeberrie gneiss, Yilgarn Craton, Western Australia: An early Archean migmatite. Precambrian Research, 78, 165–178.
Kita, N.T., Ushikubo, T., Fu, B., and Valley, J.W. (2009) High precision SIMS oxygen isotope analyses and the effect of sample topography. Chemical Geology, 264, 43–57.
Krogh, T.E. (1982) Improved accuracy of U-Pb zircon ages by the creation of more concordant systems using an air abrasion technique. Geochimica et Cosmochimica Acta, 46, 637–649.
Krogh, T.E., and Davis, G.L. (1975) Alteration in zircons and differential dissolution of altered and metamict zircon. Carnegie Institute of Washington Yearbook, 74, 619–623.
Kunicki, T.C., Beerman, D., Geiser, B.G., Oltman, E., O'Neill, R.W., and Larson, D.J. (2006) Atom probe data reconstruction, visualization and analysis with the Imago Visualization and Analysis System (IVAS). Proceedings, 19th International Vacuum Nanoelectronics Conference and 50th International Field Emission Symposium, 535–536.
Kusiak, M.A., Whitehouse, M.J., Wilde, S.A., Nemchin, A.A., and Clark, C. (2013a) Mobilization of radiogenic Pb in zircon revealed by ion imaging: Implications for early Earth geochronology. Geology, 41, 291–294.
Kusiak, M.A., Whitehouse, M.J., Wilde, S.A., Dunkley, D.J., Menneken, M., Nemchin, A.A., and Clark, C. (2013b) Changes in zircon chemistry during Archean UHT metamorphism in the Napier Complex, Antarctica. American Journal of Science, 313, 933–967.
Larson, D.J., Alvis, R.A., Lawrence, D.F., Prosa, T.J., Ulfig, R.M., Reinhard, D.A., Clifton, P.H., Gerstl, S.S.A., Bunton, J.H., Lenz, D.R., Kelly, T.F., and Stiller, K. (2008) Analysis of bulk dielectrics with atom probe tomography. Microscopy and Microanalysis, 14, 1254–1255.
Larson, D.J., Geiser, B.P., Prosa, T.J., Gerstl, S.S.A., Reinhard, D.A., and Kelly, T.F. (2011) Improvements in planar feature reconstructions in atom probe tomography. Journal of Microscopy, 243, 15–30.
Larson, D.J., Prosa, T.J., Ulfig, R.M., Geiser, B.P., and Kelly, T.F. (2013a) Local Electrode Atom Probe Tomography: A user's guide, pp. 318. Springer, New York.
Larson, D.J., Gault, B., Geiser, B.P., De Geuser, F., and Vurpillot, F. (2013b) Atom probe tomography spatial reconstruction: Status and directions. Current Opinion in Solid State and Materials Science, 17, 236–247.
Li, W., Kluth, P., Schauries, D., Rodriguez, M.D., Lang, M., Zhang, F., Zdorovets, M., Trautman, C., and Ewing, R.C. (2014) Effect of orientation on ion track formation in apatite and zircon. American Mineralogist, 99, 1127–1132.
Ludwig, K.R. (2001a) A User's Manual for Isoplot/Ex 2.49. Berkley Geochronology Center Publication no. 1a.
——— (2001b) SQUID 1.02, A User's Manual. Berkeley Geochronology Center Special Publication no. 2.
Lumpkin, G.R., and Ewing, R.C. (1988) Alpha-decay damage in minerals of the pyrochlore group. Physics and Chemistry of Minerals, 16, 2–20.
Marquis, E.A., and Hyde, J.M. (2010) Applications of atom-probe tomography to the characterisation of solute behaviour. Materials Science and Engineering R, 69, 37–62.
Mattinson, J.M. (2005) Zircon U-Pb chemical abrasion ("CA-TIMS") method: Combined annealing and multi-step partial dissolution analysis for improved precision and accuracy of zircon ages. Chemical Geology, 220, 47–66.
Miller, M.L., and Ewing, R.C. (1993) Image simulation of partially amorphous materials. Ultramicroscopy, 48, 203–237.
Miller, M.K., and Kenik, E.A. (2004) Atom probe tomography: A technique for nanoscale characterization. Microscopy and Microanalysis, 10, 336–341.
Miller, M.K., Cerezo, A., Hetherington, M.G., and Smith, G.D.W. (1996) Atom Probe Field Ion Microscopy. Oxford University Press, U.K, pp. 310.
Miller, M.K., Russell, K.F., Thompson, K., Alvis, R., and Larson, D.J. (2007) Review of atom probe FIB-based specimen preparation methods. Microscopy and Microanalysis, 13, 428–436.
Murakami, T., Chakoumakos, B.C., Ewing, R.C., Lumpkin, G.R., and Weber, W.J. (1991) Alpha-decay event damage in zircon. American Mineralogist, 76, 1510–1532.
Nasdala, L., Pidgeon, R.T., and Wolf, D. (1996) Heterogeneous metamictization of zircon on a microscale. Geochimica et Cosmochimica Acta, 60, 1091–1097.
Nasdala, L., Beran, A., Libowitzky, E., and Wolf, D. (2001a) The incorporation of hydroxyl groups and molecular water in natural zircon ($ZrSiO_4$). American Journal of Science, 301, 831–857.
Nasdala, L., Wenzel, M., Vavra, G., Irmer, G., Wenzel, T., and Kober, B. (2001b) Metamictisation of natural zircon: Accumulation versus thermal annealing of radioactivity-induced damage. Contributions to Mineralogy and Petrology, 141, 125–144.
Nasdala, L., Zhang, M., Kempe, U., Panczer, G., Gaft, M., Andrut, M., and Plötze, M. (2003) Spectroscopic methods applied to zircon. Reviews in Mineralogy and Geochemistry, 53, 427–467.
Nelson, D.R., Robinson, B.W., and Myers, J.S. (2000) Complex geological histories extending for 4.0 Ga deciphered from xenocryst zircon microstructures. Earth and Planetary Science Letters, 181, 89–102.
Nemchin, A.A., Pidgeon, R.T., and Whitehouse, M.J. (2006) Re-evaluation of the origin and evolution of >4.2 Ga zircons from the Jack Hills metasedimentary rocks. Earth and Planetary Science Letters, 244, 218–233.
O'Neill, R.W., Larson, D.J., Thompson, K., Kunicki, T.C., and Geiser, B. (2006) Measuring the roughness of buried interfaces in nanostructures by local electrode atom probe (LEAP®) analysis. Microscopy and Microanalysis, 12, 1746–1747.
Page, F.Z., Fu, B., Kita, N.T., Fournelle, J., Spicuzza, M.J., Schulze, D.J., Viljoen, V., Basei, M.A.S., and Valley, J.W. (2007) Zircons from kimberlites: New insights from oxygen isotopes, trace elements, and Ti in zircon thermometry. Geochimica et Cosmochimica Acta, 71, 3887–3903.
Palenik, C.S., Nasdala, L., and Ewing, R.C. (2003) Radiation damage in zircon. American Mineralogist, 88, 770–781.
Panayi, P. (2012) Curved reflectron. U.S. Patent No. 8,134,119 and U.K. 0509638.3.
Parrish, R.R., and Noble, S.R. (2003) Zircon U-Th-Pb geochronology by isotope dilution—thermal ionization mass spectrometry (ID-TIMS). Reviews in Mineralogy and Geochemistry, 53, 183–213.
Peck, W.H., Valley, J.W., Wilde, S.A., and Graham, C.M. (2001) Oxygen isotope ratios and rare earth elements in 3.3 to 4.4 Ga zircons: Ion microprobe evidence for high $\delta^{18}O$ continental crust and oceans in the Early Archean. Geochimica et Cosmochimica Acta, 65, 4215–4229.
Pidgeon, R.T. (1992) Recrystallization of oscillatory zoned zircon: some geochronological and petrological implications. Contributions to Mineralogy and Petrology, 110, 463–472.
——— (2014) Zircon radiation damage ages. Chemical Geology, 367, 13–22.
Pidgeon, R.T., and Wilde, S.A. (1998) The interpretation of complex zircon U-Pb systems in Archaean granitoids and gneisses from the Jack Hills, Narryer Gneiss Terrane, Western Australia. Precambrian Research, 91, 309–332.
Pidgeon, R.T., O'Neil, J.R., and Silver, L.T. (1966) Uranium and lead isotopic stability in a metamict zircon under experimental hydrothermal conditions. Science, 154, 1538–1540.
Pidgeon, R.T., Furfaro, D., Kennedy, A.K., Nemchin, A.A., Van Bronswijk, W., and Todt, W.A. (1994) Calibration of zircon standards for the Curtin SHRIMP II. In Eighth International Conference on Geochronology, Cosmochronology and Isotope Geology: U.S. Geological Survey Circular, 1107, 251.
Pidgeon, R.T., Nemchin, A.A., and Cliff, J. (2013) Interaction of weathering solutions with oxygen and U-Pb isotopic systems of radiation-damaged zircon from an Archean granite, Darling Range Batholith, Western Australia. Contributions to Mineralogy and Petrology, 166, 511–523.
Rayner, N., Stern, R.A., and Carr, S.D. (2005) Grain-scale variations in trace element composition of fluid-altered zircon, Acasta Gneiss Complex, northwestern Canada. Contributions to Mineralogy and Petrology, 148, 721–734.
Reddy, S.M., Timms, N.E., Trimby, P., Kinny, P.D., Buchan, C., and Blake, K. (2006) Crystal-plastic deformation of zircon: A defect in the assumption of chemical robustness. Geology, 34, 257–260.
Rios, S., Salje, E.K.H., Zhang, M., and Ewing, R.C. (2000) Amorphization in zircon: evidence for direct impact damage. Journal of Physics: Condensed Matter, 12, 2410–2412.
Rumble, D., Bowring, S., Iizuka, I., Komiya, T., Lepland, A., Rosing, M.T., and Ueno, Y. (2013) The oxygen isotope composition of Earth's oldest rocks and evidence of a terrestrial magma ocean. Geochemistry Geophysics Geosystems, 14, 1929–1939.
Salje, E.K.H., Chrosch, J., and Ewing, R.C. (1999) Is "metamictization" of zircon a phase transition? American Mineralogist, 84, 1107–1116.
Serizawa, A., and Miller, M.K. (2013) Radius dependence of solute concentration estimates of simulated ultrafine precipitates. Microscopy Research and Technique, 76, 1196–1203.
Shannon, R.D. (1976) Revised effective ionic radii and systematic studies of interatomic distances in halides and chalcogenides. Acta Crystallographica, A, 32, 751–767.
Silver, L.T. (1963) The relation between radioactivity and discordance in zircons.

National Academy of Science Publication, 1075, 34–39.
Silver, L.T., and Deutsch, S. (1963) Uranium-lead isotopic variations in zircons: A case study. Journal of Geology, 71, 721–758.
Smye, K.M., Brigden, C., Vance, E.R., and Farnum, I. (2014) Quantification of α-particle damage in zircon. American Mineralogist, 99, 2095–2104.
Snoeyenbos, D., Jercinovic, M.J., Reinhard, D.A., and Hombourger, C. (2012) Characterization of minerals of geochronological interest by EPMA and atom probe tomography. American Geophysical Union Abstract, V23C-2830.
Stephenson, L.T., Moody, M.P., Gault, B., and Ringer, S.P. (2011) Estimating the physical cluster-size distribution within materials using atom-probe. Microscopy Research and Technique, 74, 799–803.
Strickland, A., Miller, E.L., and Wooden, J.L. (2011a) The timing of Tertiary metamorphism and deformation in the Albion-Raft River-Grouse Creek metamorphic core complex, Utah and Idaho. The Journal of Geology, 119, 185–206.
Strickland, A., Miller, E.L., Wooden, J.L., and Valley, J.W. (2011b) Syn-extensional plutonism and peak metamorphism in the Albion-Raft-River-Grouse Creek metamorphic core complex. American Journal of Science, 311, 261–314.
Trachenko, K., Dove, M.T., and Salje, E.K. (2002) Structural changes in zircon under α-decay irradiation. Physical Review B, 65, 180102.
——— (2003) Large swelling and percolation in irradiated zircon. Journal of Physics: Condensed Matter, 15, L1–L7.
Trachenko, K., Dove, M.T., Geisler, T., Todorov, I., and Smith, B. (2004) Radiation damage effects and percolation theory. Journal of Physics: Condensed Matter, 16, S2623–S2627.
Trail, D., Mojzsis, S.J., Harrison, T.M., Schmitt, A.K., Watson, E.B., and Young, E.D. (2007) Constraints on Hadean zircon protoliths from oxygen isotopes, Ti-thermometry, and rare earth elements. Geochemistry, Geophysics, Geosystems, 8, Q06014.
Tsong, T.T., Kinkus, T.J., and Ai, C.F. (1983) Field induced and surface catalyzed formation of novel ions: A pulsed-laser time-of-flight atom-probe study. Journal of Chemical Physics, 78, 4763–4775.
Ushikubo, T., Kita, N.T., Cavosie, A.J., Wilde, S.A., Rudnick, R.L., and Valley, J.W. (2008) Lithium in Jack Hills zircons: Evidence for extensive weathering of Earth's earliest crust. Earth and Planetary Science Letters, 272, 666–676.
Utsunomiya, S., Palenik, C.S., Valley, J.W., Cavosie, A.J., Wilde, S.A., and Ewing, R.C. (2004) Nanoscale occurrence of Pb in an Archean zircon. Geochimica et Cosmochimica Acta, 68, 4679–4686.
Utsunomiya, S., Valley, J.W., Cavosie, A.J., Wilde, S.A., and Ewing, R.C. (2007) Radiation damage and alteration of zircon from a 3.3 Ga porphyritic granite from the Jack Hills, Western Australia. Chemical Geology, 236, 92–111.
Valley, J.W. (2003) Oxygen isotopes in zircon. Reviews in Mineralogy and Geochemistry, 53, 343–385.
——— (2010) Magmatic zircons: Evolution of $\delta^{18}O$ through time—Revisited in situ. Goldschmidt Conference, Geochimica et Cosmochimica Acta, Suppl, 74, A1069.
Valley, J.W., and Graham, C.M. (1991) Ion microprobe analysis of oxygen isotope ratios in metamorphic magnetite-diffusion reequilibration and implications for thermal history. Contributions to Mineralogy and Petrology, 109, 38–52.
Valley, J.W., and Kita, N.T. (2009) In situ oxygen isotope geochemistry by ion microprobe. In M. Fayek, Ed., Secondary Ion Mass Spectrometry in the Earth Sciences. Mineralogical Association of Canada Short Course 41, 19–63.
Valley, J.W., Chiarenzelli, J., and McLelland, J.M. (1994) Oxygen isotope geochemistry of zircon. Earth and Planetary Science Letters, 126, 187–206.
Valley, J.W., Peck, W.H., King, E.M., and Wilde, S.A. (2002) A cool early Earth. Geology, 30, 351–354.
Valley, J.W., Lackey, J.S., Cavosie, A.J., Clechenko, C.C., Spicuzza, M.J., Basei, M.A.S., Bindeman, I.N., Ferreira, V.P., Sial, A.N., King, E.M., and others. (2005) 4.4 billion years of crustal maturation: Oxygen isotopes in magmatic zircon. Contributions to Mineralogy and Petrology, 150, 561–580.
Valley, J.W., Ushikubo, T., and Kita, N.T. (2007) In situ analysis of three oxygen isotopes and OH in ALH 84001: Further evidence of two generations of carbonates. Lunar and Planetary Science Conference, 38, abstract no.1147.
Valley, J.W., Ushikubo, T., Strickland, A., Reinhard, D.A., Snoeyenbos, D., Lawrence, D., Martin I., Kelly T.F., and Cavosie, A.C. (2012) Elemental and Isotopic tomography at single-atom-scale in 4.0 and 2.4 Ga zircons. Fall Meeting, American Geophysical Union, San Francisco, abstract no. V12A-05.
Valley, J.W., Cavosie, A.J., Ushikubo, T., Reinhard, D.A., Lawrence, D.F., Larson, D.J., Clifton, P.H., Kelly, T.F., Wilde, S.A., Moser, D.E., and Spicuzza, M.J. (2014a) Hadean age for a post-magma ocean zircon confirmed by atom-probe tomography. Nature Geoscience, 7, 219–223.
Valley, J.W., Spicuzza, M.J., and Ushikubo, T. (2014b) Correlated $\delta^{18}O$ and [Ti] in Lunar zircons: A terrestrial perspective for magma temperatures and water content on the Moon. Contributions to Mineralogy and Petrology, 167, 956, http://dx.doi.org/10.1007/s00410-013-0956-4.
Vurpillot, F., De Geuser, F., Da Costa, G., and Blavette, D. (2004) Application of Fourier transform and autocorrelation to cluster identification in the three-dimensional atom probe. Journal of Microscopy, 216, 234–240.
Wang, X.-L., Coble, M., Valley, J.W., Shu, X.-J., Kitajima, K., Spicuzza, M.J., and Sun, T. (2014) Influence of radiation damage on Late Jurassic zircons from Southern China: Evidence from in situ measurements of oxygen isotopes, laser Raman, U-Pb ages, and trace elements. Chemical Geology, 389, 122–136.
Watson, E.B., Wark, D.A., and Thomas, J.B. (2006) Crystallization thermometers for zircon and rutile. Contributions to Mineralogy and Petrology, 151, 413–433.
Weber, W.J., Ewing, R.C., and Wang, L.M. (1994) The radiation-induced crystalline-to-amorphous transition in zircon. Journal of Materials Research, 9, 688–698.
White, L.T., and Ireland, T.R. (2012) High-uranium matrix effect in zircon and its implications for SHRIMP U-Pb age determinations. Chemical Geology, 306, 78–91.
Whitehouse, M.J., and Kamber, B.S. (2002) On the overabundance of light rare earth elements in terrestrial zircons and its implication for Earth's earliest magmatic differentiation. Earth and Planetary Science Letters, 204, 333–346.
Wilde, S.A., Valley, J.W., Peck, W.H., and Graham, C.M. (2001) Evidence from detrital zircons for the existence of continental crust and oceans on the Earth 4.4 Gyr ago. Nature, 409, 175–178.
Williams, I.S. (1998) U-Th-Pb geochronology by ion microprobe. In M.A. McKibben, W.C. Shanks III, and W.I. Ridley, Eds., Applications of microanalytical techniques to understanding mineralizing processes. Reviews in Economic Geology, 7, 1–35.
Zhang, M., Salje, E.K., Farnan, I., Graeme-Barber, A., Daniel, P., Ewing, R.C., Clark, A., and Leroux, H. (2000) Metamictization of zircon: Raman spectroscopic study. Journal of Physics: Condensed Matter, 12, 1915–1925.
Zhang, M., Salje, E.K., and Ewing, R.C. (2002) Infrared spectra of Si-O overtones, hydrous species, and U ions in metamict zircon: Radiation damage and recrystallization. Journal of Physics: Condensed Matter, 14(12), 3333–3352.

Manuscript received July 17, 2014
Manuscript accepted December 15, 2014
Manuscript handled by Adam Kent

Appendix 1

Rotating three-dimension images by APT of Y and Pb for zircon JH4.4 (specimen size ~100 × 100 × 1000 nm). See Figure 12.

App1a. JH4.4, 1000 nm, all Y atoms

App1b. JH4.4, 1000 nm, Y atoms in clusters defined at >3 at% Y

App1c. JH4.4, 100 nm, all Y atoms

App1d. JH4.4, 100 nm, Y atoms in clusters defined at >3 at% Y

App1e. JH4.4, 100 nm, all Pb atoms

App1f. JH4.4, 100 nm, Pb atoms in clusters defined at >3 at% Y

App1g. JH4.4, 100 nm. Y and Pb atoms in clusters defined at >3 at% Y

App1h. JH4.4, 100 nm, clusters defined at >3 at% Y

App1i. JH4.4, single cluster, Y = red, ^{206}Pb = teal, ^{207}Pb = orange

Appendix 2

Rotating three-dimension images by APT of Y and Pb for zircon ARG2.5 (specimen size ~100 × 100 × 250 nm). See Figures 15a–15c.

App2a. ARG2.5, all Y atoms

App2b. ARG2.5, all Pb atoms

App2c. ARG2.5, all atoms of Y (red) and Pb (teal)